

# Galaxy luminosity functions at redshifts 0.6 – 1.2 in the Chandra Deep Field South

M. Sharma<sup>1\*</sup>, M. J. Page<sup>1</sup>, A. A. Breeveld<sup>1</sup>

<sup>1</sup>*Mullard Space Science Laboratory, University College London, Holmbury St Mary, Dorking, Surrey, RH5 6NT, UK*

Accepted 2022 January 14; Received 2021 December 22; in original form 2021 October 28

## ABSTRACT

We present the rest-frame Ultra–Violet (UV) galaxy luminosity function (LF) and luminosity density (LD) measurements in the far-UV (1500 Å) wavelength, in the redshift range  $z = 0.6 - 1.2$ . The UV LF is derived using *XMM-Newton* Optical Monitor (XMM-OM), ultraviolet (1600 – 4000 Å) observations of the Chandra Deep Field South, over an area of 396 arcmin<sup>2</sup>. Using the deep UV imaging of the CDFS, we identified > 2500 galaxies in our sample with  $UVW1_{AB} \leq 24.5$  mag. This sample along with various other catalogues containing redshift information, is used to calculate the binned representation of the galaxy UV LF in the two redshift bins  $0.6 \leq z < 0.8$  and  $0.8 \leq z < 1.2$ , having a wide range of 1500 Å rest-frame UV magnitudes ( $\Delta M_{1500} \simeq 3$ ), reaching  $\simeq 1 - 1.5$  magnitudes fainter than previous studies at similar redshifts. The binned LF is described well by the Schechter function form. Using maximum-likelihood the Schechter function is fitted to the unbinned data to obtain the best-fit values of the the UV galaxy LF parameters. We find that characteristic magnitude  $M^*$  brightens by 0.8 mag from  $z = 0.7$  to  $z = 1$ , implying an increase in the star formation activity between these redshifts, as reported by past studies. Our estimate of the faint-end slope  $-1.10^{+0.19}_{-0.18}$  is on the shallower side compared with previous studies at  $z = 0.7$ , whereas a value of  $-1.56^{+0.19}_{-0.18}$  estimated for  $z = 1.0$ , agrees with previous results given the uncertainties.

**Key words:** galaxies: evolution - ultraviolet: galaxies - ultraviolet: luminosity function - galaxies: luminosity function

## 1 INTRODUCTION

Luminosity is one of the characteristic global properties of a galaxy, mainly controlled by other important quantities (e.g. the total mass, gas mass, stellar population etc. in the galaxy). Using multi-wavelength imaging surveys along with spectroscopic or photometric redshifts, luminosity can be estimated at various rest-frame wavelengths. These estimates can be used to produce a one-point statistic called the luminosity function (LF) – the number density of galaxies as a function of luminosity. The LF can be used to obtain a relative distribution of power (produced at a given rest-frame wavelength) among galaxies of different luminosities and masses at a particular average epoch in the history of the Universe.

The observed functional form of galaxy LFs is different from what is predicted from the  $\Lambda$ -CDM model (assuming a mass to light ratio), both in normalisation and the shape at the bright and faint ends (e.g. Cole et al. 2001; Yang et al.

2003; Behroozi et al. 2010). This observation has led to a suggestion that there must be additional physical processes involved, causing moderation of the star formation at high and low luminosity regimes through baryonic feedback mechanisms (Moster et al. 2010). In particular, stellar feedback - outflows from supernovae (SNe) only (e.g. Dekel & Silk 1986; White & Frenk 1991) or winds from hot young stars in addition to SNe (e.g. Springel & Hernquist 2003; Oppenheimer & Davé 2006; Hopkins et al. 2012, 2014; Gatto et al. 2017) are thought to dictate the shape at low-luminosities, whereas feedback from active galactic nuclei - through relativistic outflows countering the cooling flows in cluster atmospheres (e.g. Silk & Rees 1998; King 2003; Murray et al. 2005; Croton et al. 2006; Bower et al. 2006) are thought to be responsible for the LF shape at high luminosities (see Cattaneo et al. 2009; Fabian 2012; Harrison et al. 2018, for reviews). It is clear that the functional form of the galaxy LF encodes information about these physical processes (i.e. feedback, gas accretion, mergers, etc.) dictating galaxy formation and evolution (e.g. Cole et al. 2000; Benson et al. 2003; Somerville & Davé 2015, and references therein). So, constraining this

\* E-mail: mnushv@gmail.com (MS)

functional form at different redshifts is very important to gain insights into the properties of the galaxy populations at those redshifts. The evolution of the LF parameters with redshift can be used to understand the evolutionary history of a class of galaxies under consideration.

A single-aged star-forming population produces half of its bolometric radiation during the first 1 per cent of its total lifetime (see e.g. [Leitherer et al. 1999](#)). Its bolometric luminosity is dominated by UV emission, coming from young and massive stars with very short lifetimes (see [Madau & Dickinson 2014](#)). This instantaneous star-formation feedback regulates the faint-end slope of the UV LF, as it occurs, unlike other longer wavebands, where the LFs are shaped by accumulative feedback taking place over very long time scales. Therefore, rest-frame UV is considered an important tracer for instantaneous star-formation rate density (SFRD), although affected by dust (see [Kennicutt & Evans 2012](#)). This is also one of the reasons why the LF in the rest-frame UV has emerged as a key diagnostic for studying the evolution of galaxies and contribution of these galaxies towards cosmic star formation rate density (see [Madau & Dickinson 2014](#)).

In the recent history of the field, many studies used data from spaceborne and/or ground based observatories to produce estimates of the galaxy LF in different redshift ranges (up to  $z = 10$ ). Some of these works use drop-out techniques along with various colour selection criterion to identify the sources and estimate photometric redshifts (e.g. [Yoshida et al. 2006](#); [Dahlen et al. 2007](#); [Ouchi et al. 2009](#); [Oesch et al. 2010](#); [Bouwens et al. 2015](#); [Bowler et al. 2015](#); [Mehta et al. 2017](#); [Stefanon et al. 2017](#)), while others derive their photometry in the rest-frame band of interest using model fits to the spectral energy distribution (SED) by combining photometry in different wave bands (e.g. [Gabasch et al. 2004](#); [Dahlen et al. 2007](#); [Bowler et al. 2015](#); [Parsa et al. 2016](#); [Cucciati et al. 2012](#); [Moutard et al. 2020](#)). Some studies use their photometry with redshifts from other surveys (e.g. [Arnouts et al. 2005](#); [Wyder et al. 2005](#); [Hathi et al. 2010](#); [Hagen et al. 2015](#)). Recently some works have tried to use gravitational lensing to get to extremely faint absolute magnitudes (e.g. [Alavi et al. 2016](#); [Bhatawdekar et al. 2019](#)).

In the redshift range ( $z \leq 1.5$ ), the UV LF can be estimated from data obtained from the *GALEX* (*Galaxy Evolution Explorer*; [Martin et al. 2005](#)) satellite. Using rest-frame 1500 Å broad-band photometry from the *GALEX* FUV filter (1750 – 2800 Å), the UV LF parameters were obtained at low redshifts by [Wyder et al. \(2005\)](#) and [Budavári et al. \(2005\)](#). The NUV filter on *GALEX* was used for studying the UV LF of galaxies at  $0.2 \leq z \leq 1.2$  in [Arnouts et al. \(2005\)](#). A relatively flat faint-end slope (see eq. 8),  $\alpha \simeq -1.2$ , was reported by these works at low redshifts ( $z < 0.4$ ). However, they calculated a steep and almost constant value,  $\alpha \simeq -1.6$ , in the redshift range  $0.6 \leq z \leq 1.2$  (e.g. [Arnouts et al. 2005](#); [Wyder et al. 2005](#)). Using the Early Release Science data of the GOODS - South field (Great Observatories Origins Deep Survey; [Giavalisco et al. 2004](#)) from the WFC3/UVIS instrument on board the *Hubble Space Telescope* (*HST*), [Oesch et al. \(2010\)](#) obtained the faint-end slope,  $\alpha = -1.52 \pm 0.25$  in the redshift interval  $0.5 < z < 1$ . [Hagen et al. \(2015\)](#) have calculated the UV LF in the redshift range  $0.2 < z < 1.2$ , using data from UV/Optical Telescope (UVOT; [Roming et al. 2005](#)) on-board the *Neil Gehrels Swift Observatory* ([Gehrels et al. 2004](#)), in the Chandra Deep Field South (CDFs; [Gi-](#)

[aconi et al. 2001](#)). They have used U-band selection with UV photometry at shorter wavelengths. Their values of the UV LF parameters are within  $1\sigma$  of [Arnouts et al. \(2005\)](#). [Page et al. \(2021\)](#) used the UVW1 filter of the Optical/UV telescope, the *XMM-Newton* Optical Monitor (XMM-OM; [Mason et al. \(2001\)](#)) on-board the *XMM-Newton* observatory, and derived the 1500 Å UV LF from observations of the 13 Hr field.

Some authors have derived UV LFs at  $z < 1.2$  by selecting galaxies at longer wavelengths and extrapolating their SEDs to rest-frame FUV. In [Gabasch et al. \(2004\)](#), the *I*-band selected data set from the FORS Deep Field are employed to calculate a range of values  $-1.14 < \alpha < -0.96$  for redshifts  $0.45 < z < 1.1$ . [Cucciati et al. \(2012\)](#) have used *I<sub>AB</sub>*-band selected data and measured  $\alpha$  to be in the range  $-1.17 \pm 0.05$  to  $-0.91 \pm 0.16$  for the redshift range  $0.3 < z < 1.1$  using the VVDS Survey. Another recent work covering our redshift range is [Moutard et al. \(2020\)](#). They used a large data-set from *CFHT* Large Area U-band Deep Survey (CLAUDS; [Sawicki et al. 2019](#)) and HyperSuprime-Cam Subaru Strategic Program (HSC-SSP; [Aihara et al. 2018](#)) for their LF estimates. They also re-analysed the *GALEX* data to measure the UV LF at redshift  $z < 0.9$ . The above mentioned three works calculate galaxy LFs to higher redshifts and we only quote their results falling within the redshift range of our study (i.e.  $z < 1.2$ ).

In this paper we use observations of the Chandra Deep Field South (CDFs) from the UVW1 filter on XMM-OM. The UVW1 filter on the XMM-OM has a central wavelength 2900 Å and samples the 1500 Å flux better than *GALEX* at redshift  $z = 1$  where the *GALEX* NUV pass-band is too blue, and the rest frame 1500 Å UV radiation is placed at the tail of the filter. In addition to that, the full width at half-maximum (FWHM) of the point spread function (PSF) for *GALEX* NUV filter is  $\simeq 5$  arcsec ([Morrissey et al. 2007](#)). This big PSF puts its data at higher risk to source confusion as compared to UVW1 data obtained at a sharper PSF of  $\simeq 2^1$  arcsec. *HST* solves this problem as it has excellent resolution, but covers a very small sky area, so its data might be prone to cosmic variance. So, in this redshift range, XMM-OM can be used to put better constraints on the UV LF parameters over larger fields than covered by the *HST* UV instrumentation and at a better spatial resolution compared with *GALEX*. We mainly compare our results to [Arnouts et al. \(2005\)](#); [Hagen et al. \(2015\)](#) and [Page et al. \(2021\)](#) as they use the similar redshift binning scheme and direct rest-frame FUV observations for their LF estimates.

The rest of this paper is structured as follows. The observations, data and the reduction process are explained in section 2. In section 3 we discuss the completeness simulations, possible biases and source-confusion. The cross-correlations to the ancillary data, which include the spectroscopic and photometric redshifts are used to identify the sources in section 4. Various corrections are made to the data in section 5, before final analysis. In the following section 6, we discuss the methods to construct the UV LF and derive the LF parameters. Then, in section 7, we mention the possible impacts of cosmic variance on our calculations.

<sup>1</sup> [https://xmm-tools.cosmos.esa.int/external/xmm\\_user\\_support/documentation/uhb/XMM\\_UHB.html](https://xmm-tools.cosmos.esa.int/external/xmm_user_support/documentation/uhb/XMM_UHB.html)

Section 8 contains the calculations for the luminosity density. The results are presented in section 9, and their implications are discussed in section 10. Finally, we conclude this paper in section 11. Throughout the paper we adopt a flat cosmology with  $\Omega_\Lambda = 0.7$ ,  $\Omega_M = 0.3$  and Hubble's constant  $H_0 = 70 \text{ km s}^{-1} \text{ Mpc}^{-1}$ . The distances (and volumes) are calculated in comoving co-ordinates in Mpc (and  $\text{Mpc}^3$ ). We use the AB system of magnitudes (Oke & Gunn 1983).

## 2 OBSERVATIONS & DATA

### 2.1 XMM-OM observations of the CDFS

The Chandra Deep Field South (CDFS) : one of the deepest observation sites of the Chandra X-ray Observatory (Luo et al. 2008), has been a target of many space and ground-based observation campaigns in different wavebands. It is centred on RA 3h 32m 28.0s DEC  $-27^\circ 48' 30''$  (J2000.0) (Rosati et al. 2002). This field is popular for having very low HI column density (Stark et al. 1992), hence allows very deep observations.

The main aim of the *XMM-Newton* survey in the Chandra Deep Field South (XMM-CDFS) was to detect and study the X-ray spectral properties of obscured X-ray sources. The field was observed for more than 3 Ms to acquire good quality X-ray spectra for heavily obscured AGN, at all possible redshifts (Comastri et al. 2011).

In addition to the X-ray instruments, the *XMM-Newton* observatory carries the XMM-OM, an optical/UV telescope with a primary task to complement the X-ray observations. It is a very capable stand-alone instrument with a wavelength coverage in the range 180 – 590 nm over six broadband filters, a fine PSF  $\simeq 2''$  (FWHM) for each filter, over the entire field of view (FOV) spanning  $17 \times 17 \text{ arcmin}^2$  (for more details see Mason et al. 2001). We refer to Table 1 and Fig. 1 in Page et al. (2012) for other properties of the XMM-OM filter pass-bands. More details about the different image configurations can be found in the *XMM-Newton* User's Handbook<sup>2</sup>. XMM-OM can be used to take observations in the optical/UV regimes and build source catalogues in most fields observed by *XMM-Newton*. We use the data from the UVW1 filter, which is the most relevant to derive the 1500 Å LF at the redshifts we are interested in. Our catalogue of the XMM-CDFS Deep Survey consists of 30 *XMM-Newton* observations in six different observational epochs between July 2001 and February 2010. There are 11 observations corresponding to 2 epochs, acquired with the XMM-OM in 'full frame low-resolution' configuration to obtain single exposures of the whole FOV in  $2 \times 2$  binned resolution giving pixel size of 0.95 arcsec (Mason et al. 2001). These full-frame images have exposure durations of 5 ks each. There are 17 other observations spanning 4 epochs that were acquired in 'default' (also known as 'rudi-5') configuration, where a setup of 5 consecutive exposures is used to cover 92 per cent of the FOV with the same binning and pixel scale as full-frame mode. In the rudi-5 exposures, UVW1 observations have an exposure duration ranging from 0.8 – 5 ks. One observation

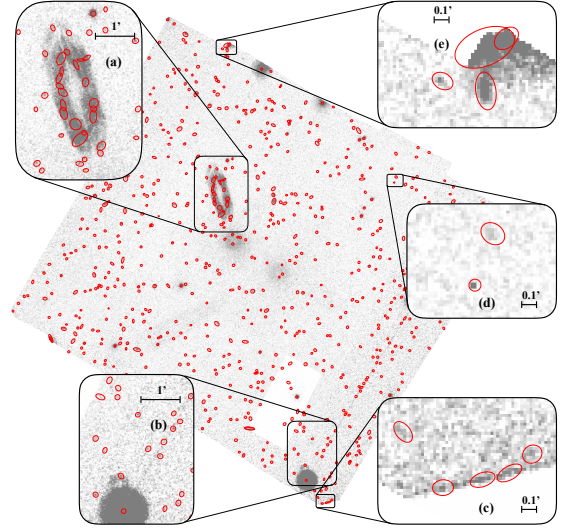


**Figure 1.** Example image created by mosaicing two different exposures of UVW1 images of the CDFS. These exposures are processed using the standard SAS tasks without any additional processing. All the detections by OMDETECT are shown by red ellipses. At the center of the image the scattered background light structures (explained in section 2.2) are also clearly visible as two circular enhancements corresponding to both the exposures. Other features of the XMM-OM images, anti-clockwise from top-left: (a) loops caused by internal reflection inside the telescope; (b) read-out streak for bright sources; (c, e) false detections at the corners; (d) cosmic ray bit-flips at different locations in the image.

contains exposures in both configurations (see Table 1 and also Antonucci et al. 2015, for details of observations).

### 2.2 XMM-OM data reduction and processing

The XMM-OM data were obtained from the *XMM-Newton* Science Archive<sup>3</sup> (XSA). The reduction and processing were carried out using version 17 of the standard *XMM-Newton* Science Analysis System<sup>4</sup> (SAS) tools.

The SAS script OMICHAIN is designed to execute various SAS tasks on the UVW1 images. These tasks include operations like obtaining the tracking history of the telescope movement, flat-fielding, correcting for modulo-8 (mod-8) noise, source-detection and photometry. Later into the chain, quality maps are created, the images are projected onto the sky plane and aspect correction is done for the source-lists and the sky-images (see Page et al. 2012, for details about the tasks making up the chain).

We start with removing the cosmic rays from the raw images before they are fed to the OMICHAIN. The detector counts from a source are saved as a 16-bit number in the instrument memory. A high energy cosmic ray passing through the instrument may cause a high bit in the memory to flip

<sup>2</sup> [https://xmm-tools.cosmos.esa.int/external/xmm\\_user\\_support/documentation/uhb/XMM\\_UHB.html](https://xmm-tools.cosmos.esa.int/external/xmm_user_support/documentation/uhb/XMM_UHB.html)

<sup>3</sup> <https://www.cosmos.esa.int/web/xmm-newton/xsa/>

<sup>4</sup> <https://www.cosmos.esa.int/web/xmm-newton/sas>

**Table 1.** Here we tabulate the UVW1 observations of the CDFS from XMM-OM. First two columns are observation ID (OBS ID), Epoch (Observation dates). Third column lists the configurations in which the observation were taken (i.e. whether ‘full-frame’ (ff), ‘rudi5’ (r5) or both (r5 + ff) as explained in section 2.1). The following columns represent the pointing sky co-ordinates RA and DEC (in degrees) and the Exposure time (Exp. time) in kilo-seconds.

OBS ID	Epoch	Configuration	RA (deg)	DEC (deg)	Exp. time (ks)
0108060501	2001-07-28	r5	03h 32m 29.29s	-27d 48' 40.0"	1.48
0108060601	2002-01-13	ff	03h 32m 27.99s	-27d 48' 50.0"	5.0
0108060701	2002-01-15	r5 + ff	03h 32m 26.70s	-27d 48' 40.0"	10.0
0108061801	2002-01-16	ff	03h 32m 27.99s	-27d 48' 30.0"	5.0
0108061901	2002-01-17	ff	03h 32m 27.99s	-27d 48' 10.0"	5.0
0108062101	2002-01-20	ff	03h 32m 29.29s	-27d 48' 20.0"	5.0
0108062301	2002-01-23	ff	03h 32m 27.99s	-27d 48' 10.0"	5.0
0555780101	2008-07-05/06	r5	03h 32m 42.29s	-27d 45' 05.0"	8.8
0555780201	2008-07-07/08	r5	03h 32m 42.29s	-27d 45' 35.0"	8.8
0555780301	2008-07-09/10	r5	03h 32m 39.99s	-27d 45' 35.0"	8.5
0555780401	2008-07-11/12	r5	03h 32m 39.99s	-27d 45' 05.0"	8.8
0555780501	2009-01-07	ff	03h 32m 25.00s	-27d 49' 25.0"	4.0
0555780601	2009-01-11	ff	03h 32m 25.00s	-27d 49' 55.0"	4.0
0555780701	2009-01-13	ff	03h 32m 25.00s	-27d 50' 25.0"	4.0
0555780801	2009-01-17	ff	03h 32m 22.70s	-27d 49' 25.0"	4.0
0555780901	2009-01-19	ff	03h 32m 22.70s	-27d 49' 55.0"	4.0
0555781001	2009-01-23	ff	03h 32m 22.70s	-27d 50' 25.0"	3.5
0555782301	2009-01-25	ff	03h 32m 22.70s	-27d 50' 25.0"	3.5
0604960301	2009-07-05/06	r5	03h 32m 42.29s	-27d 46' 09.0"	10.0
0604960201	2009-07-14/18	r5	03h 32m 39.99s	-27d 45' 35.0"	7.12
0604960101	2009-07-27/28	r5	03h 32m 42.29s	-27d 45' 35.0"	10.0
0604960401	2009-07-29/30	r5	03h 32m 39.99s	-27d 46' 07.0"	7.0
0604961101	2010-01-05	r5	03h 32m 25.00s	-27d 48' 52.3"	10.0
0604961201	2010-01-09	r5	03h 32m 22.30s	-27d 46' 09.0"	5.0
0604960701	2010-01-13	r5	03h 32m 22.70s	-27d 49' 25.0"	10.0
0604961301	2010-01-20	r5	03h 32m 25.00s	-27d 49' 25.0"	2.6
0604960601	2010-01-27	r5	03h 32m 25.00s	-27d 49' 55.0"	10.0
0604960801	2010-02-06	r5	03h 32m 22.30s	-27d 50' 31.0"	8.1
0604961001	2010-02-14	r5	03h 32m 22.70s	-27d 49' 55.0"	9.0
0604961801	2010-02-18	r5	03h 32m 22.59s	-27d 49' 34.7"	9.0

and increase the count significantly and trigger a false detection (Fig. 1(d)) during photometry which in the end may add spurious sources to the catalogue. We used code developed by Pych (2004) to remove most of the cosmic rays. This code leaves some less significant bit-flip effects in our images, which were removed manually.

The cosmic-ray-corrected raw images were processed by OMICHAIN up to the mod-8 correction step, after which they were taken out of the pipeline for additional corrections on top of the standard SAS data processing. First we got rid of the background scattered light feature at the center of the image (Fig. 1). It was removed by using a template made using multiple UVW1 images from different fields as explained in Page et al. (2021). Second, the readout streaks (if any) coming out of the bright sources (Fig. 1(b)) were corrected. The readout streaks are formed by photons arriving during frame transfer of the CCD (Page et al. 2017). These are removed by subtracting the excess count rate of the affected columns from the images. The loopy artefacts shown in Fig. 1(a), come from reflection of bright stars outside the field of view by a chamfer in the detector window housing inside the telescope (Mason et al. 2001). These artefacts were re-

moved by masking the loops in the corresponding images and applying the same masks for individual exposure maps.

After correcting for all the artefacts, the images were then distortion corrected<sup>5</sup>, aligned with the equatorial coordinate frame of COMBO-17 (Wolf et al. 2004, 2008) then rotated and re-binned into sky coordinates using the SAS task OMATT. A mosaiced UVW1 image was created from individually processed images by using the SAS task OMMOSAIC. The resulting image is shown in Fig. 2. The edges of the final UVW1 image are the regions of minimum exposure times and hence maximum noise. There is a possibility that noise spikes get detected as sources in these regions of low S/N, giving rise to false detections. To avoid these this, we masked the pixels having an exposure time less than 5 ks (which is equivalent to removing a total area of  $\simeq 6.43$  arcmin<sup>2</sup>). Our corrected image covers a total area  $\simeq 395$  arcmin<sup>2</sup>. The mosaiced UVW1 image was then fed to the SAS task OMDetect, which performs photometry and source detection, using dedicated algorithms for identifying point and extended sources. A range of apertures from 2.8 to

<sup>5</sup> This corrects for the small offsets of the pixel position from a linear scale (Mason et al. 2001)

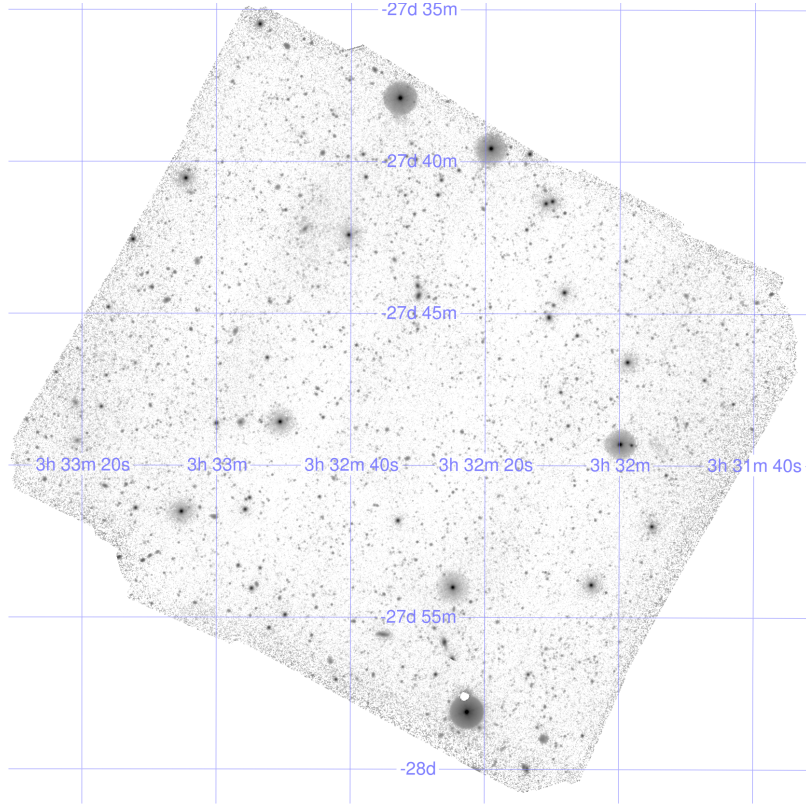


**Figure 2.** The UVW1 mosaiced image of the CFDS covering a sky-area of  $\simeq 395 \text{ arcmin}^2$ . It is obtained by co-adding 13 full-frame and 170 rudi-5 exposures of the CFDS.

5.7 arcsec are used based on brightness of individual sources as well as their proximity on the image. We refer to Page et al. (2021) and Page et al. (2012) for the details on the source detection. We finally end up with a UVW1 source-list containing 3277 sources at  $3\sigma$ .

### 3 EDDINGTON BIAS, CONFUSION AND COMPLETENESS

#### 3.1 Eddington bias and flux boosting

There is a likelihood for a source to get confused with another source in a densely packed region of the field or it might not be detected at all due to limitations in the source detection algorithm. Therefore, once the final image is produced, it is necessary to precisely quantify different biases and determine the level of confusion in the data that are used to construct luminosity functions.

The errors in the photometric flux measurement give rise to the Eddington bias (Eddington 1913). Due to measurement errors, more faint magnitude sources are scattered into slightly brighter (or less faint) magnitude bins, compared to sources of slightly brighter magnitudes that are being scattered into fainter magnitude bins. This causes an overestimate in the number of faint sources and biases the calculations towards their luminosities. Precise estimation of this bias is more important for galaxies close to the detection limits.

#### 3.2 Source confusion

In a densely packed region of the image, two or more sources may be so close that they can not be distinguished individually. Such sources could get identified as a single bright source because of their accumulative flux. There is a chance that these false detections get incorrectly identified with counterparts in other catalogues and end up in the final source-list hampering the final results. This effect increases with the number of detections and hence sensitivity of the instrument. Note for comparison that Ly et al. (2009) calculated an incompleteness of 21 per cent due to source confusion in the *GALEX* NUV filter.

In order to quantify the combined effect of the biases and confusion, we calculate the completeness of a sample as a function of magnitude.

#### 3.3 Completeness simulations

We define completeness as - the fraction of sources detected as a function of the magnitude. Completeness of a survey goes down with decreasing signal to noise. For example at the edges of the images, because of the low S/N ratio, some sources are missed by the detection algorithm.

To estimate the completeness of our sample, we use a common technique used in blank field studies : we simulate artificial galaxies having properties similar to real galaxies, randomly distribute these synthetic galaxies on the image, and detect them using the same detection process that we use to create the UVW1 source-list.

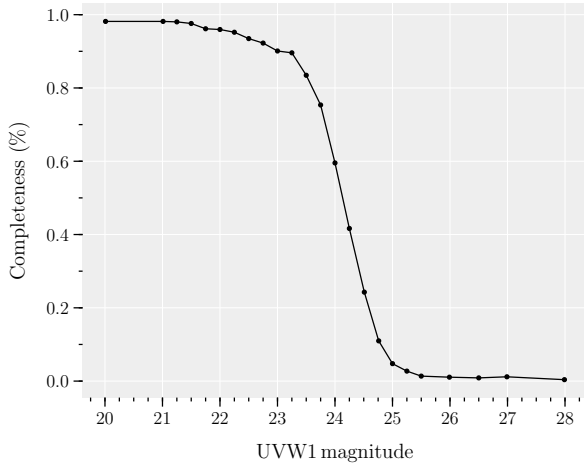


**Figure 3.** Completeness of the source detection as a function of UVW1 magnitude, as determined from the simulations described in section 3.3. The black data points represent the fraction of recovered simulated galaxies at each input UVW1 mag.

We simulate 1000 point sources at each input magnitude ranging from UVW1 mag 21 to 25.5 in steps of 0.25 mag. We extend the range to UVW1 20 mag on the brighter side. In order to simulate the effect of Eddington bias close to the flux limit of the survey, and to better assess the source-confusion, we further extend the magnitude range to UVW1 mag 28.0 with wider step sizes. The sources are inserted in the image at random positions one at a time, and if a source is detected less than 1 arcsec away from the inserted source position, it is considered retrieved.

We obtain three pieces of information from the simulations: 1) The fraction of the injected sources successfully recovered is recorded for a given magnitude. We use this fraction as a measure of ‘*completeness*’. The fraction of recovered sources as a function of UVW1 magnitude is plotted in Fig. 3. The completeness measure is included in our calculations as shown in section 6. 2) The ‘*confusion limit*’ of the survey is the magnitude beyond which the source detection process cannot be trusted due to large source-confusion. We measure the degree of source confusion at the magnitude limit of our survey to see if it is confusion limited. It can be seen from Fig. 3, that the fraction of recovered sources drops steeply before the curve asymptotically flattens at the level of 1.5 per cent, which we consider to be the level of source confusion in our image. This implies that the sensitivity of the detector falls off and the survey reaches a sensitivity limit before it becomes limited by confusion. 3) We also obtain an ‘*error distribution*’ from these simulations which records the distribution of magnitude difference between the injected and recovered sources. Fig. 4 shows the error histograms at each input magnitude as a function of magnitude offset between the injected and recovered sources. This error distribution is later incorporated into our calculations while fitting the Schechter function to the data using maximum likelihood (for details see section 6.2). The completeness curve informs our choice of appropriate survey depth - the faint magnitude limit beyond which no sources were included in our calculations to produce a binned LF and to estimate the Schechter function parameters in section 6.1 and 6.2.

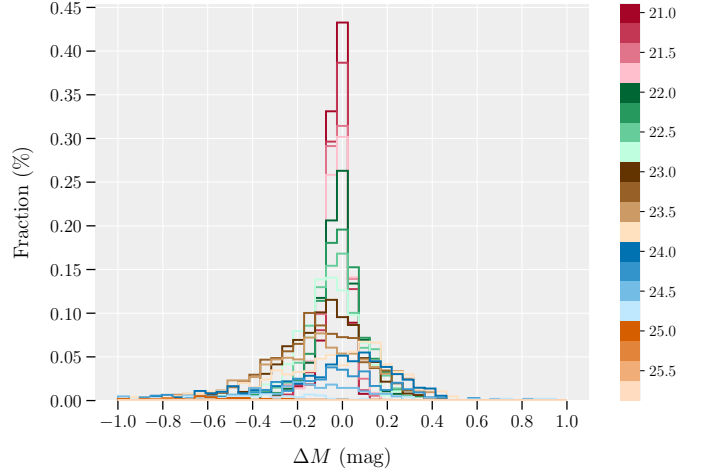


**Figure 4.** The estimated distribution of the magnitude errors in the detection process at each simulated UVW1 magnitude. Each histogram represents the distribution of offsets of the recovered magnitudes from the simulated input magnitudes. The simulated UVW1 input magnitudes are shown by different colours scaled according to the color-bar at the right.

From the completeness measurements, our catalogue is found to be > 97 per cent complete for UVW1 magnitude  $\leq 21.5$  and 80 per cent complete at UVW1 magnitude = 23.6. The completeness falls below 10 per cent at UVW1 magnitude 24.75 and below 5 per cent for UVW1 25 mag (Fig. 3). Beyond this magnitude the recovery of sources starts becoming insensitive to the input magnitude. It can also be seen from Fig. 4, that at UVW1 25 mag almost all the detections are fainter sources riding positive noise excursions. The completeness goes further down to  $\simeq 1.5$  per cent for UVW1 magnitudes fainter than 25.5 mag (Fig. 3). We consider 25.5 mag to be the faintest possible detection limit for our survey. As we go fainter, beyond UVW1 25.5 mag, in Fig. 3 we are more likely to detect sources because of source confusion than because of faint real sources on top of noise spikes.

From this analysis we conclude here that our survey becomes insensitive at UVW1 25.5 mag, before it becomes confusion limited. In fact with more exposure time on the CDFS, we could have a survey that goes deeper in UVW1 magnitudes. To make sure we have a very secure UVW1 source-list, make a conservative cut at UVW1 magnitudes 24.5 (one magnitude brighter than the detection limit) as the magnitude limit for our survey, where the probability of detecting a source is 15 times the underlying level of source confusion. This magnitude limit corresponds to UVW1 mag 24.46 after considering the effect of Galactic foreground extinction explained in section 5.1.

#### 4 CROSS-CORRELATIONS TO ANCILLARY DATA

The UVW1 source-list is cross-correlated with various catalogues to acquire some additional information on the sources, primarily redshifts. An appropriate matching radius for the cross-correlation is needed for that purpose or else a very low matching radius may produce an inadequate number

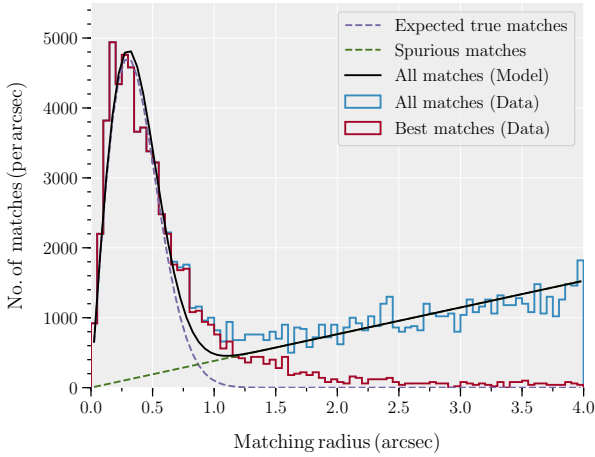


**Figure 5.** The distribution of angular offsets between all detected sources in the UVW1 source-list and their closest counterparts in the COMBO-17 catalogue is represented by the red histogram. The offset distribution of all the matches found in COMBO-17 for each source in the UVW1 source-list is represented by blue histogram. The bin size of 0.05 arcsec is used for both histograms. The black solid line is the expected model obtained by simultaneously fitting a Rayleigh distribution (dotted purple curve) and a line (dotted green curve) to the distribution of offsets w.r.t. all matches.

of matches and a large matching radius may give rise to unwanted spurious matches with other catalogues. We first determine an appropriate matching radius by comparing the expected and observed distribution of cross-correlated sources. The ancillary data from other catalogues is summarised next. We then conclude this section by using the ancillary data to assign redshifts to our sources, and also identify and remove any bright AGN or stars present in the source-list.

#### 4.1 Spurious cross-correlations

We match our UVW1 source-list to the COMBO-17 (Wolf et al. 2004, 2008) catalogue, with a variable angular offset up to 5 arcsec. The distributions of angular offsets corresponding to a best match (closest counterpart within the offset limit) and all matches (all counterparts within the offset limit) are plotted in Fig. 5. These distributions are plotted in blue and red solid lines respectively, with the x-axis truncated to 4 arcsec offsets.

A Rayleigh distribution is predicted for the probability distribution of the angular offsets, given that the uncertainties in their positions have a Gaussian distribution (Page et al. 2012). The number of spurious matches (false counterparts) should grow linearly as a function of matching radius. The total expected distribution of matches (actual as well as spurious) is obtained by combining the Rayleigh distribution corresponding to the actual sources and a straight line corresponding to unrelated matches. This distribution as a function of offsets ( $x$ ) should take the form,

$$D(x) = A \frac{x}{\sigma^2} \exp\left(-\frac{x^2}{2\sigma^2}\right) + mx. \quad (1)$$

This predicted distribution of all offsets is fitted to the distri-

bution of all matches, with  $A$ ,  $\sigma$ , and  $m$  as free parameters. The fitted model is represented by the solid black line in Fig. 5. The dashed purple curve is the Rayleigh distribution fit and the straight line is plotted in dashed green. The fit parameters values are  $2330 \pm 60$  sources,  $0.299 \pm 0.006$  arcsec and  $382.2 \pm 14.6$  sources per square arcsec for  $A$ ,  $\sigma$ , and  $m$  respectively.

It is clear from Fig. 5 that, the modelled distribution of true matches drops asymptotically after 1 arcsec matching radius, and the ratio of number of spurious to true matches grows rapidly after that. So, 1 arcsec seems to be reasonable choice for a cross-matching offset radius.

In order to assess the quality of the cross-correlation for our best matches and to gauge the likelihood that the matched sources happen to be within the error radius of the UVW1 sources just by chance, we use Monte-Carlo simulations. We simulate a random sample of linearly distributed offsets up to a maximum offset of 1 arcsec from the fitted straight line. Another random sample of potential matches is simulated from the true (Rayleigh) source distribution of all matches within the offset of 1 arcsec. These samples are compared to each other and we note the number of spurious offsets, smaller than the expected true offsets, and consider only this number of actual spurious sources may make their way into our source-list. Using these simulations we find that  $77 \pm 13$  (3 per cent) out of total 2544 matches, will really be spurious. The errors are 95 per cent confidence intervals obtained through bootstrap re-sampling. So adopting 1 arcsec as the offset radius will give rise to 3 per cent of the total matched sources being spurious. An important remark needs to be added here : we have ignored clustering of faint sources. Since we have compared our catalogue with a deeper ground based survey, the background source distribution will be dominated by sources that are fainter than the UVW1 detected sources. For the case when there is a closer, but fainter background source than the correct counterpart, within an arcsec, it is quite likely that the fainter source will not even be detected and the correct counterpart will be chosen. So, the actual fraction of sources that are matched spuriously will be smaller than 3 per cent. We think it is a reasonable compromise, and adopt 1 arcsec as the offset radius when we cross-correlate our catalogue with other catalogues unless stated otherwise.

#### 4.2 Ancillary data

Our final image extends outside the CDFS as defined by the Chandra X-ray survey, so our ancillary data also includes surveys targeting the Extended-CDFS (E-CDFS Lehmer et al. 2005) in addition to those exclusively from CDFS. The E-CDFS has been covered by almost 50 bands from UV to mid-infrared (MIR) (see Table 1 and 2 in Hsu et al. (2014)) in different surveys.

We will briefly summarise the catalogue and surveys used in this work. Hsu et al. (2014) used photometry from UV to MIR to estimate the photometric redshifts in the E-CDFS. We use their catalogue for spectroscopic and photometric redshifts. We also use the VLT<sup>6</sup> master catalogue of spectroscopic redshifts compiled from various spectroscopic

<sup>6</sup> the details can be found at <http://www.eso.org/sci/>

campaigns in the CDFS up until 2012-13. (Le Fèvre et al. 2005; Szokoly et al. 2004; Mignoli, M. et al. 2005; Ravikumar et al. 2007; Vanzella et al. 2008; Balestra et al. 2010; Silverman et al. 2010; Ravikumar et al. 2007). FIREWORKS (Wuyts et al. 2008) is a  $K$ -band selected catalogue for the CDFS, containing photometry in several bands. It provides both photometric and spectroscopic redshifts. The catalogue provided by Rafferty et al. (2011) is the source of most of the photometric redshift used in this work. This catalogue is constructed using 7 different (see Appendix A.1 in Rafferty et al. (2011)) catalogues in the E-CDFS to derive the photometric redshifts. The COMBO-17 survey imaged CDFS with the Wide Field Imager at the MPG/ESO 2.2m telescope, in 17 passbands to obtain photometric redshifts for galaxies identified at  $R_{\text{Vega}} < 24$ . (Wolf et al. 2004, 2008). The MUSYC survey, which used photometry in 32 bands to estimate redshifts in the E-CDFS (Cardamone et al. 2010; Taylor et al. 2009) also contributes a few photometric redshifts to our catalogue. The Gaia DR2 (Gaia Collaboration et al. 2018) is the second data release catalogue from observations of the Gaia observatory. We use it to identify the stars in our source-list.

### 4.3 Cross-correlation to optical and mid-infrared counterparts

Here we match our source-list with the ancillary data listed in the previous sub-section, using the 1 arcsec radius deduced in sub-section 4.1. We start with removing the stars and then obtain the redshifts for our sources. We remove bright AGN present in the catalogue at the end.

#### 4.3.1 Stars

The presence of stars in the source-list is irrelevant to the extra-galactic UVLF. The CDFS is known for its isolated position towards the Galactic halo, where the stellar population is comparatively aged, so the UVW1 sample will have little contamination from Galactic stars. Nevertheless we cross correlated our catalogue with the Gaia DR2 (Gaia Collaboration et al. 2018) to identify the stars by matching it with our source-list and removing sources with significant proper motions. COMBO-17 data were also employed to remove any stars from the source-list. They used stellar templates from different libraries to identify the stars. We removed 155 sources identified as stars in total, leaving 3122 sources.

#### 4.3.2 Redshifts

Once the stars were removed we cross-matched the remaining sources with the redshift catalogues. Most of our spectroscopic redshifts are from the Hsu et al. (2014) catalogue. We obtain more than 1400 spectroscopic redshifts from their catalogue. The VLT master catalogue provides 212 spectroscopic redshifts. The FIREWORKS catalogue is used only

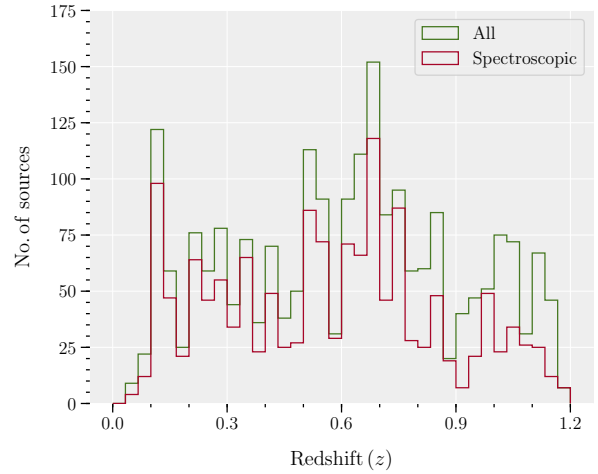


**Figure 6.** Redshift distribution of the CDFS sample. The spectroscopic redshifts are represented in red colour and total number is shown in green.

for its spectroscopic redshifts. Appropriate quality flags provided by each catalogue have been used to apply conservative quality cuts (see Table 2), in order to make sure we get the most accurate redshifts. Regarding the photometric redshifts, Rafferty et al. (2011) contributes 838 photometric redshifts. This is followed by catalogues from COMBO-17 and MUSYC surveys providing 68 and 28 redshifts, respectively. We used the Hsu et al. (2014) catalogue again to acquire 66 photometric redshifts in addition to the spectroscopic ones. We applied a quality cut to only allow photometric redshifts for which the 68 per cent confidence region around the peak redshift has a width  $< 0.2$ . The list of all the catalogues used for redshifts with references, number of contributed redshifts and the quality cuts can be found in Table 2.

#### 4.3.3 Active Galactic Nuclei

The accretion discs around the central super-massive black holes in active galaxies are known to emit large quantities of UV radiation, which dominates the UV flux coming from star formation in these galaxies. The inclusion of these galaxies with UV bright active galactic nuclei (AGN) in the sample can cause erroneous estimation of the UV LF. These sources affect the shape of the UV LF especially at the bright end because very bright galaxies are extremely rare. The CDFS has a significant number of bright AGN in the redshift range of our interest, that can contaminate the UVW1 sample. Assuming that AGN bright in UV fluxes will also have X-ray emission, the X-ray catalogues from Xue et al. (2016) and Luo et al. (2017) are used to identify the AGN present in our sample. Any bright AGN making their way into the sample were removed by using a luminosity cut-off  $10^{42}$  ergs  $\text{s}^{-1}$  in the full x-ray band (0.5 - 8 KeV). We make detailed checks on the effect of AGN contamination on our sample in the redshift range we explore, in Appendix A.

After removing the potential AGNs, a sample of 2518 galaxies is selected with redshifts of the highest quality, 1559 of which are spectroscopic. The redshift distribution of our final galaxy sub-sample truncated to redshift 1.2 is shown in Fig. 6. A section of the source-list is presented in Table



**Table 2.** Catalogues used for spectroscopic and photometric redshifts, along with the number of redshifts and quality flags (QF) used for each catalogue.  $z_{68}$  represents the 68 percent confidence interval around each photometric redshift in the photometric catalogues.

Source Catalogue	Number <sup>a</sup>	QF
Spectroscopic redshifts		
Hsu et al. (2014)	1403	0,1
Le Fèvre et al. (2005)	30	3,4
Szokoly et al. (2004)	38	2
Mignoli, M. et al. (2005)	21	1
Ravikumar et al. (2007)	34	2
Vanzella et al. (2008)	17	A
Balestra et al. (2010)	63	A
Silverman et al. (2010)	9	2
Kurk et al. (2013)	6	1
Wuyts et al. (2008)	3	1
Photometric redshifts		
Rafferty et al. (2011)	832	$z_{68} < 0.2$
Hsu et al. (2014)	66	$z_{68} < 0.2$
Wolf et al. (2008)	46	$z_{68} < 0.2,$ $R < 24$ mag
Cardamone et al. (2010)	17	$z_{68} < 0.2,$ QF $\leq 1$
Taylor et al. (2009)	13	$z_{68} < 0.2$
Santini et al. (2015)	1	$z_{68} < 0.2,$ QF = 0

<sup>a</sup>Represents the numbers before the bright AGN are removed.

**Table 3.** The UVW1 source list used for this paper. The positions and apparent UVW1 AB magnitudes are calculated using `omdetect` (see section 2), the redshifts are obtained by cross-matching with other catalogues (see section 4 and Table 2). The full table is available in the machine readable form with the online version of the paper.

RA (J2000) deg	DEC (J2000) deg	$z$	UVW1 mag
53.2170	-27.7417	0.80	21.42
53.0706	-27.6580	1.00	21.76
53.2845	-27.8815	0.74	21.91
53.0778	-27.6676	0.61	21.93
53.1258	-27.8849	0.64	22.00

3 and the full table of sources ( $z = 0.6 - 1.2$ ) in machine readable form is available online.

## 5 CORRECTIONS

### 5.1 Galactic foreground extinction

The radiation coming from extra-galactic objects is absorbed and/or scattered by the interstellar dust in the Milky way. As a result, the incoming light is extinguished by a certain magnitude. Galactic extinction for a given photometric band is given by,  $A_\lambda = k(\lambda) E(B - V)$ , where  $k(\lambda)$  is the extinction coefficient determined by the Galactic extinction curve (Cardelli et al. 1989) and  $E(B - V)$  is determined from the dust map of the sky.

We use an all-sky dust extinction map from Schlegel et al. (1998) to obtain  $E(B - V)$ , and Table 6 from Schlafly & Finkbeiner (2011) to calibrate the above relation. The

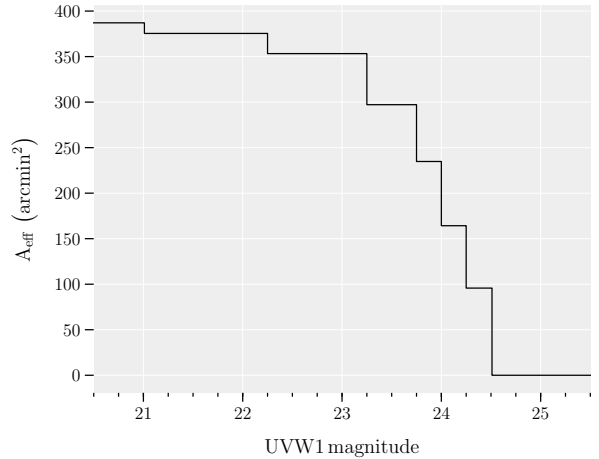


**Figure 7.** Effective area as a function of UVW1 magnitude. The completeness of the survey is taken into account using this function in the construction of binned luminosity functions as described in section 6.1.

correction for dust-extinction in the UVW1 band,  $A_{\text{UVW1}}$  is applied in equation 2 after applying the K-correction (section 5.2). Its value along the direction of CDFS is estimated to be 0.039. This low value of extinction is supported by a low value of the Galactic HI column density of around  $8.8 \times 10^{19} \text{ cm}^{-2}$  (Stark et al. 1992).

### 5.2 K correction

The observed spectral energy distributions (SEDs) appear different from the rest-frame SEDs as they are red-shifted due to the expansion of the Universe. So, the measurements taken in a particular waveband sample different parts of the SED of a galaxy, depending upon the redshift of that galaxy. Thus, when we compare galaxies in a given observed waveband (say  $[\nu_1, \nu_2]$ ) at different redshifts, we are actually looking at two different rest-frame wavebands. This effect is most severe for very distant galaxies.

To correct for this offset, we use an additive term called K-correction, while calculating the absolute magnitudes of the galaxies from apparent magnitudes. The method used to derive these K-corrections as a function of redshift from the appropriate best-fit templates is explained in detail in Page et al. (2021). Once the K-corrections  $K(z)$  are calculated, the following relation is used to calculate the absolute magnitude for each source

$$M_{1500}(z) = m - 5 \log \left( \frac{d_L(z)}{\text{Mpc}} \right) - 25 - K(z) - A_{\text{UVW1}}, \quad (2)$$

where  $d_L$  is the luminosity distance.

## 6 LUMINOSITY FUNCTION

### 6.1 Binned luminosity function

We use the Page & Carrera (2000) method to calculate the binned luminosity function. The number of galaxies  $N$ , inside a bin of the volume-magnitude space bound by redshift interval  $z_{\text{min}} < z < z_{\text{max}}$  and absolute magnitude interval

$M_{\min} < M < M_{\max}$ , is related to the differential luminosity function  $\phi(M, z)$  as

$$N = \phi(M, z) \int_{M_{\min}}^{M_{\max}} \int_{z_{\min}}^{z_{\max}} \frac{dV(z)}{dz} dz dM, \quad (3)$$

assuming that the variations of  $\phi(M, z)$  over redshift and absolute magnitude intervals are small enough to be ignored (Page & Carrera 2000). The integral on the right hand side of the above equation can be considered as the effective 4-volume  $V_{\text{bin}}$  of the volume-magnitude bin.

We divide the total survey area  $A$  into  $j$  sub-fields, and add the contribution of each sub-field towards the effective volume of the volume-magnitude bin,

$$V_{\text{bin}} = \int_{M_{\min}}^{M_{\max}} \sum_j \int_{z_{\min, j}}^{z_{\max, j}} \frac{dV(z)}{dz} dz dM, \quad (4)$$

and obtain,  $dV(z)/dz$  for each sub-field by multiplying its effective area with the differential comoving volume element,

$$\frac{dV(z)}{dz} = A_{\text{eff}, j}(M) \frac{c H_0^{-1} d_L^2}{(1+z)^2 [\Omega_\lambda + \Omega_m(1+z)^3]^{1/2}} \quad (5)$$

where,  $A_{\text{eff}}$  is the effective area of each sub-field,

$$A_{\text{eff}, j}(m) = A C_j(m) \left( \frac{\pi}{180} \right)^2. \quad (6)$$

Here  $A$  is in  $\text{deg}^2$  and  $C_j(m)$  is the completeness fraction for each sub-field. The total effective area  $A_{\text{eff}}(m)$ , plotted in Fig. 7, is a step function of apparent magnitude where the steps are the effective areas for the individual sub-fields.

The number of sources  $N_{\text{bin}}$  are counted in each bin and divided by  $V_{\text{bin}}$  to estimate the binned LF,

$$\phi = \frac{N_{\text{bin}}}{V_{\text{bin}}}. \quad (7)$$

From Poisson's statistics (Gehrels 1986), we calculate the uncertainty for  $N$  objects and hence the statistical uncertainty in the LF for each bin in the redshift-magnitude space. Because of the nature of our survey, it may also be subjected to cosmic variance, which we discuss in detail in section 7. The resulting luminosity function  $\phi$  with units of  $\text{Mpc}^{-3} \text{mag}^{-1}$ , are shown in Fig. 8

## 6.2 Schechter function parameters

To recover more information from a magnitude limited sample of galaxies, we analyse the galaxy distribution in the redshift-magnitude space by comparing it to a galaxy LF model using a maximum likelihood estimator. We adopt the Schechter function (Schechter 1976) to model the galaxy LF in each redshift bin. It can be parametrised as a function of magnitude  $M$  with parameters  $\alpha$ ,  $\phi^*$  and  $M^*$ ,

$$\phi(M) \equiv \phi(M; \alpha, \phi^*, M^*) = k \phi^* \frac{e^{k(1+\alpha)(M^*-M)}}{e^{k(M^*-M)}}, \quad (8)$$

where  $k = \frac{2}{5} \ln 10$ . The functional form at faint magnitudes is characterised by a power law slope  $\alpha$ , also called the faint-end slope. The power law form cuts off at a characteristic magnitude,  $M^*$ , and an exponential behaviour follows to brighter magnitudes.  $\phi^*$  is the normalisation. We use the maximum likelihood approach to fit the above model to our

observations. Our likelihood function for all  $N_G$  sources is defined as

$$\mathcal{L} = \prod_i^{N_G} p(M_i, z_i) \quad (9)$$

where  $p(M_i, z_i)$  is the probability density for a galaxy  $i$ , to be observed with an absolute magnitude  $M_i$  in the survey magnitude limits  $[M_{\min}, M_{\max}]$  at the object's redshift  $z_i$  in the interval  $[z_{\min}, z_{\max}]$ . It is given by

$$p(M_i, z_i) = \frac{\phi(M_i, z_i)}{\int_{M_{\min}}^{M_{\max}} \int_{z_{\min}}^{z_{\max}} \phi(M, z) \frac{dV(z)}{dz} dz dM}. \quad (10)$$

The Schechter function parameters can be found by maximising  $\mathcal{L}$ , which is equivalent (and more numerically convenient) to minimising the negative logarithm of the likelihood,

$$S = -2 \ln \mathcal{L} = -2 \sum_{i=1}^{N_G} \ln p(M_i, z_i). \quad (11)$$

It is important to note here that the normalisation  $\phi^*$  can not be fitted jointly with  $M^*$  and  $\alpha$ , using this framework as it gets cancelled out in equation 10, and the final likelihood function is independent of it. It is determined separately by asserting that the predicted and observed number of sources is equal.

The measurement errors associated with the data can seriously hamper the outcomes of the fitting process, if not properly accounted for. The effects of these errors may become more severe particularly for our Schechter function model which increases exponentially at bright magnitudes. To take into account the uncertainties, we use the error distribution (Fig. 4) derived from the completeness simulations in section 3.3. The observed galaxy LF for a population of galaxies can be obtained from the underlying LF via this error distribution. We use the formalism discussed in Page et al. (2021) to incorporate the photometric uncertainties into our calculations. A brief description of the method is given below.

If a galaxy of true absolute magnitude  $M$  is observed with an absolute magnitude in the range  $[M', M' + dM']$  with a probability  $P(M'|M) dM'$ , an underlying LF  $\phi(M)$  should be observed as a differential LF  $P(M'|M) \phi(M) dM$ . In other words, we marginalize our model over the error distribution of magnitudes  $P(M'|M)$ , instead of calculating it for single galaxy magnitudes. This can be included in the maximum likelihood method by modifying equation 10, which now becomes

$$p(M'_i, z_i) = \frac{\int \phi(M_i, z_i) P(M'|M) dM}{\int \int \int \phi(M, z) P(M'|M) dM \frac{dV(z)}{dz} dz dM'}. \quad (12)$$

We incorporate the completeness of the survey into our likelihood formalism by normalising these histograms with the number of injected sources in completeness simulations. We refer to the study by Page et al. (2021) for more details of the framework. This framework is incorporated in our work by using a Markov Chain Monte Carlo (MCMC) prescription (described in the next paragraph), whereas Page et al. (2021) use a different approach.

We minimise equation 11 and then using MCMC, we obtain the posterior probability distribution for the Schechter

function parameters around the minimum value of the likelihood. We use EMCEE (Foreman-Mackey et al. 2013) - a popular python implementation of the Affine Invariant MCMC Ensemble Sampler (Goodman & Weare 2010) to apply the MCMC. In this scheme, a likelihood function as in equation 11 can be obtained from a posterior probability distribution function given by,

$$p(\theta | M'_i, z_i) \propto p(\theta) \times p(M'_i, z_i | \theta), \quad (13)$$

where,  $\theta = (\phi^*, M^*, \alpha)$  are the model parameters, and  $M'_i$  and  $z_i$  are the the magnitude and redshift of the galaxies lying inside the redshift bin  $z_{\min} < z < z_{\max}$ . A uniform uninformative prior distribution is assumed  $p(\theta)$  for our parameters and the likelihood function is given by,  $\mathcal{L} = p(M'_i, z_i | \theta)$ .

## 7 COSMIC VARIANCE

The large-scale variations in the underlying density field of the Universe, are a major source of uncertainty in LF calculations. A higher or lower number count of galaxies will be observed in over dense or under dense regions of the Universe. This fluctuation will affect any one-point statistic based on these number counts (Somerville et al. 2004). This so called cosmic variance can significantly affect the number density of sources for surveys exploring a small volume of the Universe (Somerville et al. 2004; Moster et al. 2011). Using a simple mass to light ratio, Trenti & Stiavelli (2008) show that the effects of cosmic variance are not limited to number density, it can also be a source of additional uncertainty in calculations of characteristic magnitude of a luminosity function. We estimate the effects of cosmic variance on our calculations here.

We estimate the errors in the space density of UVW1 sources by using the prescription provided by Moster et al. (2011), which calculates the cosmic variance as function of the projected sky-area, redshift, the redshift bin size and stellar masses. We obtain the stellar masses for our galaxies by matching our source-list to the CANDELS-GOODS-S stellar mass catalogue from Santini et al. (2015). This survey covers 43 percent of our UVW1 image and contains 47 percent of our sources in the redshift range 0.6 – 1.2 using a matching radius of 1 arcsec. We find an average stellar mass of  $5.7 \times 10^9 M_\odot$  and  $6.0 \times 10^9 M_\odot$  for redshift bins centered around mean redshift 0.7 and 1.0 respectively. For these average stellar masses the average fractional cosmic variance obtained from the Moster et al. (2011) method is 0.194 for redshift bin 0.6 – 0.8 and 0.132 for redshift bin 0.8 – 1.2. We want to remark here that estimation is based on the assumption that the mean stellar masses calculated from 47 percent of the sources are representative of all the sources in the redshift range we are exploring.

There is another tool developed by Trenti & Stiavelli (2008), which can be used to estimate the effects of cosmic variance. Their work calculates cosmic variance using a different approach, wherein the average bias of the sample is calculated using the number density of the sources in synthetic surveys obtained from numerical N-body simulations. We assume  $\sigma_8$  and an average halo occupation fraction values of 0.8 and 0.5 respectively. In addition to these parameters we use the Sheth & Tormen (1999) bias formalism in the Trenti & Stiavelli (2008) web tool, and obtain  $1\sigma$  fractional

**Table 4.** Fractional errors on normalisation due to cosmic variance.

z	$\Delta\phi^*(1\sigma)$	
	Moster et al. (2011)	Trenti & Stiavelli (2008)
0.6 – 0.8	0.194	0.138
0.8 – 1.0	0.132	0.104

errors of 0.138 and 0.104 on our normalisation for redshift 0.7 and 1.0 respectively. The cosmic variance errors on the parameters, calculated using tools from both Trenti & Stiavelli (2008) and Moster et al. (2011) are tabulated in Table 4.

In their work, Trenti & Stiavelli (2008) also report the dependence of  $M^*$  on the density of the large scale environment. This dependence has important implication when comparing the shapes of the LFs in different redshift bins or contrasting the LF shapes from different surveys. We look at the implications of the cosmic variance on our results in the discussion section 8.

## 8 UV LUMINOSITY DENSITY

The luminosity function parameters can be strongly covariant, and may also depend upon the assumptions made. The integral of the UV luminosity function i.e. the total UV flux per unit comoving volume - UV luminosity density is a much more robust quantity which can be directly translated into star formation rate density. It can be defined as,

$$\rho = \int_0^\infty L \phi(L/L^*) d(L/L^*), \quad (14)$$

where  $\phi(L/L^*)$  is the Schechter function parametrized in terms of luminosity instead of magnitudes (equation 8). For galaxies brighter than  $L$ , the luminosity density can be calculated from the Schechter function parameters as,

$$\rho = \phi^* L^* \Gamma(\alpha + 2, L/L^*). \quad (15)$$

We calculate the values within a range of luminosities corresponding to  $M_{1500} = [-10, -24]$ . The resulting values are tabulated in Table 5 and also plotted in Fig. 13 along with estimates from previous studies.

## 9 RESULTS

We derived galaxy rest-frame UV LFs in the redshift range  $0.6 \leq z < 0.8$  and  $0.8 \leq z < 1.2$ , using the Page & Carrera (2000) method explained in section 6.1. Schechter functions were fitted to all the data to obtain the LF parameters as described in section 6.2. The results are plotted in Fig. 8, along with the LFs obtained from Arnouts et al. (2005), Hagen et al. (2015) and Page et al. (2021) for comparison at the same redshifts. The left and the right panels in Fig. 8 show LFs derived at the mean redshift  $z = 0.7$  and  $z = 1.0$  respectively. The faintest  $M_{1500}$  magnitudes explored by our UV LF estimates are more than one magnitude fainter than the characteristic magnitude  $M^*$  in both redshift bins.

We compare the galaxy UV LF obtained at redshifts 0.7 and 1 in Fig. 9. For comparison we have plotted the local luminosity function obtained by Wyder et al. (2005). Fig. 10 shows the one and two dimensional posterior distributions

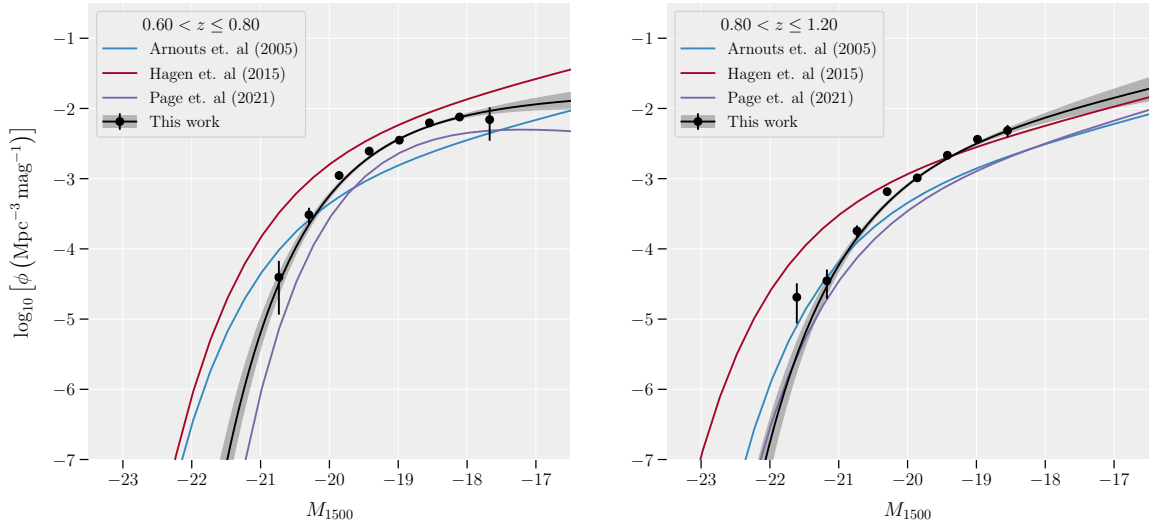


**Figure 8.** UV luminosity function of galaxies in the redshift intervals  $0.6 \leq z < 0.8$  in the left panel and  $0.8 \leq z < 1.2$  in the right panel as a function of the 1500 Å magnitude. The data points show the binned number densities measured using the Page & Carrera (2000) method. The black solid line is our best-fitting Schechter function derived from the CDFS field as described in Section 6.2. We obtain this curve from the median value of the posterior distribution of Schechter function parameters. The grey shaded area around the best-fit Schechter function represents the  $1\sigma$  (68.26 per cent) uncertainties. The blue and red and purple solid lines are the Schechter functions obtained by Arnouts et al. (2005), Hagen et al. (2015) and Page et al. (2021).

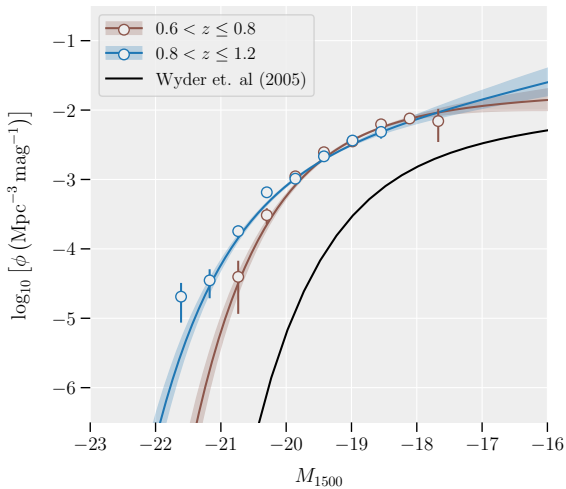


**Figure 9.** The estimated LF in this work. The UV LF at redshift  $z = 0.7$  is shown in brown colour and the UV LF at redshift  $z = 1$  is shown in blue. The solid lines, data points and the shaded areas have the same meaning as in Fig. 8. The black solid line shows the LF estimate in the local Universe from Wyder et al. (2005).

for the LF parameters, obtained by MCMC simulations. The dark and light shaded regions show the 68 and 95 per cent confidence regions for three parameters. The best fit values obtained using the maximum likelihood method presented in section 6.2 are listed in Table 5. A strong correlation can be seen in the Schechter function parameters in Fig. 10. The closed contours imply that we have sufficient data, going to faint enough magnitudes, to explore a significant fraction of the parameter space and constrain all the parameters.

It can be seen from Table 5 that our best fit value of

the faint-end slope changes by  $1.85\sigma$  as redshift increases from  $z = 0.7$  to  $z = 1$ , while the characteristic magnitude evolves significantly. A brightening of 0.8 mag at  $> 3\sigma$  in  $M^*$  is observed as the redshift increases. This is also evident in Fig. 9 where the  $1\sigma$  error regions corresponding to both LF just overlaps towards the fainter magnitudes implying an insignificant change, whereas at the bright end the error regions are well separated, and the LF (blue coloured) representing the redshift bin centered at  $z = 1$  extends towards brighter magnitudes as compared to the other (brown) LF for  $z = 0.7$ . The normalisation  $\phi^*$ , changes to become three times its value at  $z = 1$  as we move to  $z = 0.7$  (Fig. 10). It is very important to remark here that the effects of cosmic variance have to be kept in mind while looking at the changes in the LF parameter  $\phi^*$  from one redshift bin to another.

The bright ends of the LFs ( $M_{1500} < 21$  mag for  $z = 0.7$  and  $M_{1500} < 22$  mag for  $z = 1$ ) are not very well constrained. We note here that to constrain this regime of the LF properly, we need observations from a very large area of the sky to have more bright sources in the sample.

## 10 DISCUSSION

We compare the outcomes of our analysis with the literature values of the Schechter function parameters in the redshift range  $0.6 \leq z < 0.8$  and  $0.8 \leq z < 1.2$ . For comparison we tabulate previous estimates in Table 6 and plot some of these values in Fig. 11. For mean redshift  $z = 0.7$  we find that our results lie just at the edge of the  $2\sigma$  region around values reported by Arnouts et al. (2005). The faint-end slope reported by their study is  $\alpha = -1.60 \pm 0.26$ , whereas we get a flatter value  $\alpha = -1.10^{+0.19}_{-0.18}$ . As can be seen in the left panel of Fig. 8, there is a deviation from these works at

**Table 5.** Derived median Schechter function parameters of the galaxy UV LF (normalisation, characteristic magnitude and faint-end slope) from their respective posterior distributions, and the estimated value of the Luminosity density. The LF parameters are defined in equation 8 in section 4.2, and the LD in equation 14.  $N_G$  is the number of galaxies in each bin. Errors indicate  $1\sigma$  (68.26 per cent) uncertainties.

$\langle z \rangle$	$z_{\min}$	$z_{\max}$	$N_G$	$\phi^*/10^{-3}$ ( $\text{Mpc}^{-3}$ )	$M^*$	$\alpha$	$\rho/10^{26}$ ( $\text{erg s}^{-1} \text{Hz}^{-1} \text{Mpc}^{-3}$ )
0.7 <sup>a</sup>	0.60	0.80	545	$12.73^{+2.03}_{-2.25}$	$-18.84^{+0.14}_{-0.15}$	$-1.10^{+0.19}_{-0.18}$	$2.02^{+0.26}_{-0.18}$
1.0 <sup>a</sup>	0.80	1.20	534	$4.26^{+1.18}_{-1.12}$	$-19.64^{+0.16}_{-0.18}$	$-1.56^{+0.19}_{-0.18}$	$2.63^{+1.04}_{-0.55}$

<sup>a</sup>Average redshift for the bin.

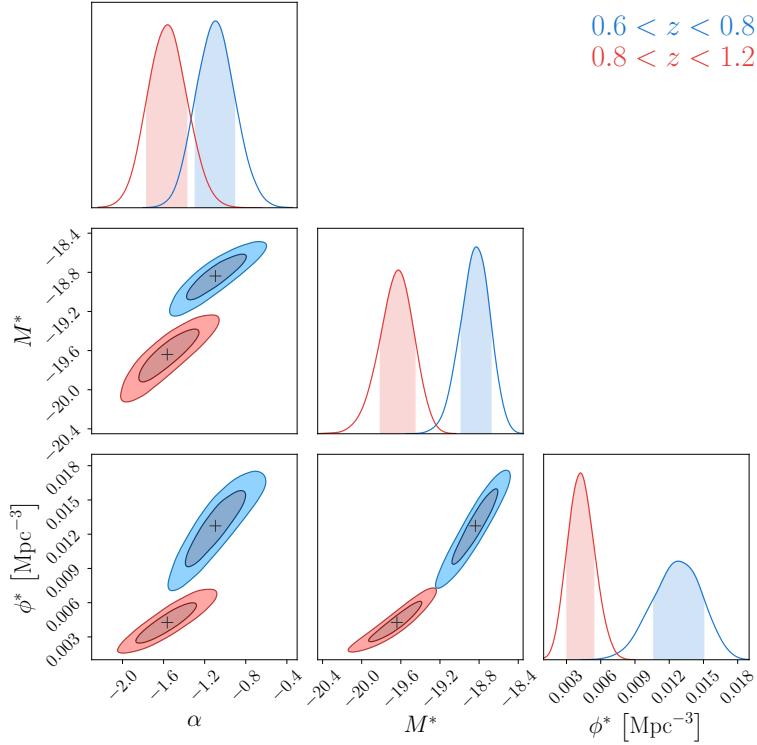


**Figure 10.** This figure represents the marginalized one dimensional (along the diagonal) and two dimensional (off-diagonal) posterior distributions of Schechter function parameters  $\alpha$ ,  $M^*$  and  $\phi^*$ . The redshift bin  $0.6 \leq z < 0.8$  is represented by blue and redshift bin  $0.8 \leq z < 1.2$  is shown in red colour. The shaded region in the dark and light coloured areas in the off-diagonal plot correspond respectively to 68 and 95 per cent confidence intervals for LF parameters. The black ‘+’ symbols represent the median values for  $\alpha$ ,  $M^*$  and  $\phi^*$ . The shaded region in the diagonal plots represent the one dimensional 68 per cent confidence region.

the bright-end as well, however we note here that a survey wider than the CDFS with more bright galaxies is required to constrain the very bright end of the LF. The best-fit characteristic magnitude  $M^*$  resulting from our analysis is about a magnitude fainter than what is inferred by [Arnouts et al. \(2005\)](#). Thanks to the exceptionally long total exposure time of our XMM-OM UVW1 image, we manage to get the best constraints to date on the faint-end slope, from a survey observing directly in the rest frame  $1500 \text{ \AA}$  at these redshifts. Compared to [Arnouts et al. \(2005\)](#), this study improves the  $1\sigma$  constraints on  $\alpha$  by 44 per cent on averaging both redshift bins, whereas the  $M^*$  uncertainties are reduced by a significant margin of 63 per cent on average.

We compare our results to [Hagen et al. \(2015\)](#), who used the observations from the same field as ours (i.e. CDFS) for their calculations, and report smaller uncertainties on  $M^*$ . It should be noted that they used U band observations from *Swift*-UVOT to select their sources. This affects the mini-

mum limiting magnitude in the rest-frame FUV band, and so the data used for their UV LF calculations do not go deep enough in the rest-frame FUV to put constraints on the faint-end slope. They fixed their faint-end slope equal to the [Arnouts et al. \(2005\)](#) values to calculate other parameters. A correlation between faint-end slope and characteristic magnitude, demands their  $M^*$  estimates to be strongly dependent on [Arnouts et al. \(2005\)](#). We want to remark here that our data reach  $\simeq 0.5 \text{ mag}$  and  $> 1.0 \text{ mag}$  deeper than [Arnouts et al. \(2005\)](#) and [Hagen et al. \(2015\)](#) respectively in this redshift bin. In Fig. 12, we plot our parameter estimates for  $M^*$  and  $\phi^*$  after fixing the faint end slope values to the ones from [Arnouts et al. \(2005\)](#), similar to [Hagen et al. \(2015\)](#). We see the confidence contours for the fixed  $\alpha$  (in yellow) shrink dramatically as compared to the ones obtained for variable  $\alpha$  (in grey) for both redshift bins. For redshifts  $0.6 \leq z < 0.8$  (upper panel in Fig. 12), the normalisation obtained by [Hagen et al. \(2015\)](#) is within  $1 \sigma$  if

**Table 6.** The derived values of the Schechter function parameters  $\phi^*$ ,  $M^*$  and  $\alpha$  from previous studies.

Work	$\langle z \rangle^a$	$\phi^*/10^{-3}$ (Mpc $^{-3}$ )	$M^*$	$\alpha$
Dahlen et al. (2007)	0.55	$6.23^{+2.68}_{-2.12}$	$-19.22^{+0.28}_{-0.28}$	$-1.39^{+0.14}_{-0.13}$
Arnouts et al. (2005)	0.7	$1.67^{+0.95}_{-0.95}$	$-19.84^{+0.40}_{-0.40}$	$-1.60^{+0.26}_{-0.26}$
Cucciati et al. (2012)	0.7	$9.53^{+0.99}_{-0.99}$	$-18.30^{+0.10}_{-0.10}$	$-0.90^{+0.08}_{-0.08}$
Hagen et al. (2015)	0.7	$6.65^{+1.21}_{-1.21}$	$-19.78^{+0.10}_{-0.10}$	$-1.60^b$
Page et al. (2021)	0.7	$10.5^{+1.20}_{-5.20}$	$-18.50^{+0.40}_{-0.60}$	$-0.70^{+1.10}_{-1.10}$
Oesch et al. (2010)	0.75	$3.01^{+1.50}_{-3.15}$	$-19.17^{+0.51}_{-0.51}$	$-1.52^{+0.25}_{-0.25}$
Weisz et al. (2014)	0.75	$3.56^{+5.25}_{-1.79}$	$-18.62^{+0.27}_{-0.21}$	$-1.23^{+0.14}_{-0.07}$
Moutard et al. (2020)	0.75	$4.40^{+0.30}_{-0.30}$	$-19.11^{+0.04}_{-0.04}$	$-1.40^{+0.04}_{-0.04}$
Cucciati et al. (2012)	0.9	$9.01^{+0.94}_{-0.96}$	$-18.70^{+0.10}_{-0.10}$	$-0.85^{+0.10}_{-0.10}$
Arnouts et al. (2005)	1.0	$1.14^{+0.76}_{-0.76}$	$-20.11^{+0.45}_{-0.45}$	$-1.63^{+0.45}_{-0.45}$
Hagen et al. (2015)	1.0	$1.36^{+0.10}_{-0.10}$	$-20.74^{+0.12}_{-0.12}$	$-1.63^b$
Page et al. (2021)	1.0	$1.20^{+0.90}_{-1.10}$	$-19.90^{+0.60}_{-0.90}$	$-1.70^{+1.20}_{-0.80}$
Cucciati et al. (2012)	1.1	$7.43^{+1.08}_{-1.15}$	$-19.00^{+0.20}_{-0.20}$	$-0.91^{+0.16}_{-0.16}$

<sup>a</sup>Average redshift for the bin.<sup>b</sup>These faint-end slope values are fixed to those obtained by Arnouts et al. (2005).

we fix the faint end slope to Arnouts et al. (2005), however there is different characteristic magnitude. This difference could be because of the different selection technique applied by Hagen et al. (2015).

Oesch et al. (2010) estimated a faint-end slope  $\alpha = -1.52 \pm 0.25$ , in the redshift range  $0.5 < z < 1$  having a mean redshift very close to ours. Their result for  $\alpha$  and the break magnitude  $M^*$  agrees with our values within  $1\sigma$ . The UV LF estimated by Page et al. (2021) in this redshift bin seems to follow the same shape as ours (Fig. 8), with a different normalisation. They also obtain a faint value for the break magnitude ( $M^* = -18.50^{+0.40}_{-0.60}$ ). However, due to a small sample size, their value is rather uncertain.

The faint-end slope deduced by Cucciati et al. (2012) and Moutard et al. (2020) in the similar redshift bin are  $-0.90 \pm 0.08$  and  $-1.40 \pm 0.04$  respectively. Thus our values in this redshift bin agree well with their values and within  $1\sigma$  and  $2\sigma$ . However, when comparing our results to these works, it must be pointed out here again that they obtained the UV LF by extrapolating their measurement to 1500 Å from longer wavelengths.

There is no tension between our faint-end slope and Weisz et al. (2014) (i.e.  $-1.23 \pm 0.14$ ) determined for a mean redshift of  $z = 0.75$ , up to  $1\sigma$ . This study used a very different method, galactic archaeology of the galaxies in the local group, to estimate the UV LF. They were able to estimate the star formation history and hence the LFs of galaxies to  $z \sim 5$ , probing very faint magnitude limits ( $M_V = -4.9$ )

In the redshift range  $0.8 \leq z < 1.2$ , again our data is  $> 1.0$  mag deeper compared with Hagen et al. (2015). With respect to Arnouts et al. (2005) our data is  $\sim 0.15$  mag deeper. Overall our values of the UV LF parameters in this redshift bin are in accordance with findings reported by Arnouts et al. (2005), with better constraints on the faint-end slope. Their estimates of  $\alpha = -1.63 \pm 0.45$  are within  $1\sigma$  from our estimate  $\alpha = -1.56^{+0.19}_{-0.18}$ . The value of the characteristic magnitude obtained in our study,  $M^* = -19.64^{+0.16}_{-0.18}$ , is in reasonable agreement with the one determined by Arnouts et al. (2005),  $M^* = -20.11 \pm 0.45$ , considering the errors. The bright-end of the LF in this redshift bin

does not match with Hagen et al. (2015), and their  $M^*$  values are beyond  $1\sigma$  of our estimate. The situation does not change much if we fix the faint-end slope to their values. From the lower panel of Fig. 12, one can see that the results obtained from our data for a fixed and variable faint-end slope match very well. This is because our fixed faint-end slope was very close to the median of our marginalised posterior distribution of  $\alpha$ . But, despite a fixed value of  $\alpha$ , the normalisation and characteristic magnitude do not match with Hagen et al. (2015), and again, we think the reason could be the different methods applied to select the sources. There is considerable discrepancy between our best-fit value of  $\alpha$  and  $M^*$  and those obtained by Cucciati et al. (2012) at  $z = 0.9$  and  $z = 1.1$ .

As apparent from Table 6 the best-fitting faint-end slope values in the literature can be as steep as  $-1.70$  and as shallow as  $-0.85$ . This variation in the values of  $\alpha$  represents a very substantial level of uncertainty in the characterisation of galaxy UV LFs. We obtain a shallow faint-end slope for redshift  $z = 0.7$ , compared to estimates from Oesch et al. (2010) and Arnouts et al. (2005). The faint-end slope reflects the contribution of the low luminosity galaxies to the LF, so, having a smaller value than previous studies suggests that there were fewer faint galaxies at this epoch in the history of the Universe than estimated by previous studies. Our data reach 1.2 mag fainter than the characteristic magnitude  $M^*$ , so, we are confident that the faint end is sampled well. Many previous works conclude a constant value of the faint-end slope between average redshift 0.7 to 1. Our values of  $\alpha$  agree with this picture as we see very modest (close to  $2\sigma$ ) change in  $\alpha$  as redshift increases to  $z = 1$ .

The uncertainties in  $\alpha$  are also followed by uncertainties in characteristic magnitude  $M^*$  (see Fig. 11 and Table 6), because of the correlation between these two parameters as apparent from Fig. 10. The characteristic magnitude  $M^*$  estimated in this work is fainter than those reported by Hagen et al. (2015) and Arnouts et al. (2005), at both redshift bins. We see an evolution in characteristic magnitude with redshift in the range we explored, which can be attributed to evolution of the population towards brighter objects as

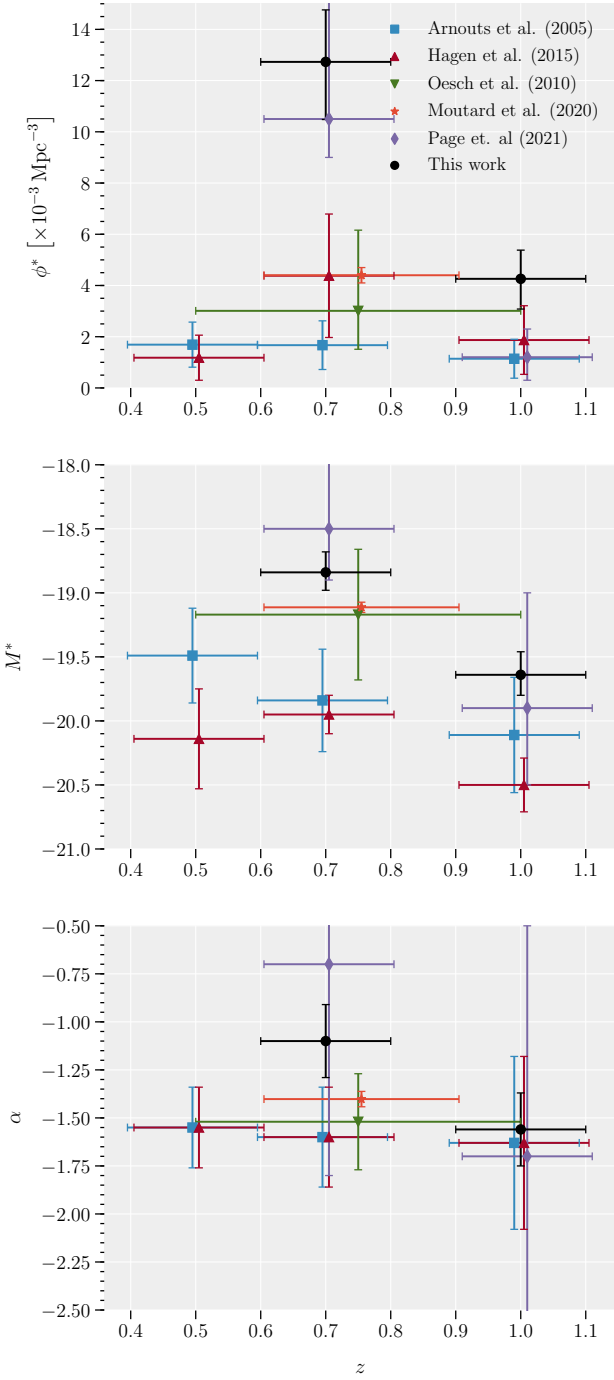


**Figure 11.** The Schechter function parameters  $\alpha$ ,  $M^*$  and  $\phi^*$ . The values estimated from this work are in black colour and other values from Arnouts et al. (2005); Hagen et al. (2015); Oesch et al. (2010); Moutard et al. (2020) and Page et al. (2021) are in blue, red, green, orange and purple colours respectively. These parameters are defined in Equation 8. The top panel represents the characteristic number density  $\phi^*$ , central panel shows characteristic magnitude  $M^*$  and the bottom panel shows the variation in faint-end slope  $\alpha$  with redshift. The horizontal error bars represent the width of the redshift bin and the vertical ones represent one  $\sigma$  (68.26 per cent) uncertainties. These values are also tabulated in Table 6. The redshifts on the horizontal axis are perturbed very slightly to clearly show the the data points separate from each other.

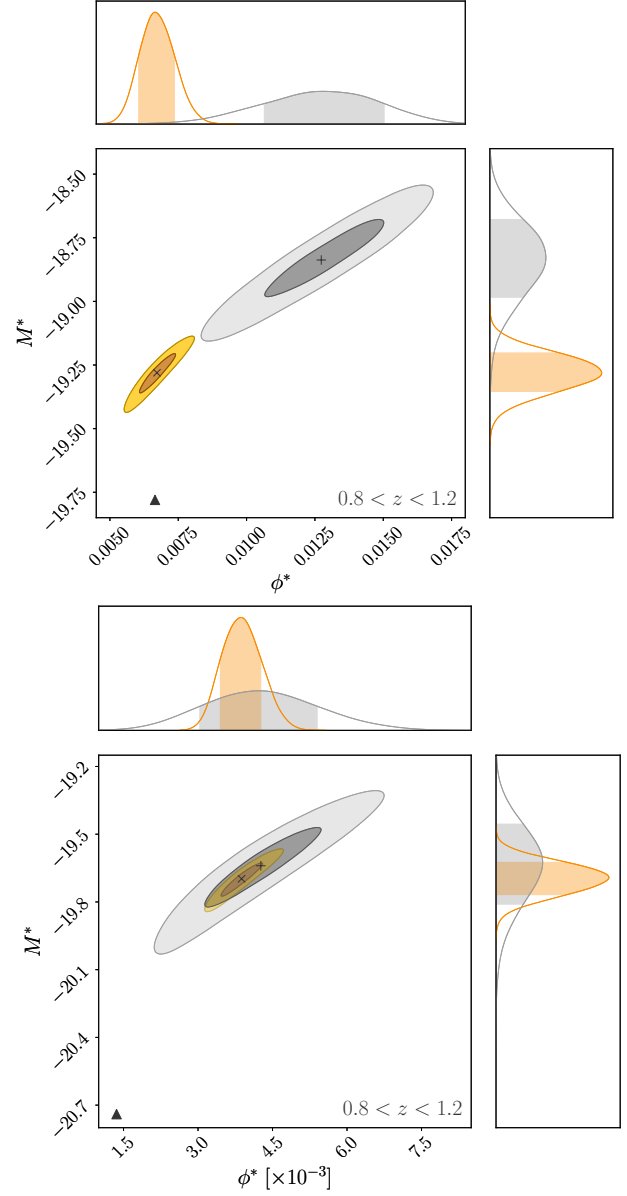


**Figure 12.** Here we plot the estimates for  $M^*$  and  $\phi^*$ . The top and bottom panels represent the redshift bins  $0.6 < z < 0.8$  and  $0.8 < z < 1.2$  respectively. ‘+’ symbols within the gray contours represent the values obtained from this work when we treat  $\alpha$  as a free parameter. ‘x’ symbols in the yellow contours represent the values from this work if we fix the faint end slope to Arnouts et al. (2005). The values obtained by Hagen et al. (2015) are shown as the upward triangle. The definitions of the contours are the same as in Fig. 10.

we get closer to the peak of the SFR in the Universe. As mentioned earlier cosmic variance needs to be considered while making any claims of the evolution of the LF parameters with redshift. Because of the presence of over-dense regions in the CDFS (Gilli et al. 2003; Dehghan & Johnston-Hollitt 2014), which lie in our 0.6–0.8 redshift bin, the space density and hence the number count of the galaxies is higher in this bin than the average of other surveys. As shown by Trenti & Stiavelli (2008), regions with above-average space density are biased towards brighter values of  $M^*$ . So, the underlying

ing value of characteristic magnitude should be fainter than our estimated value in this redshift range. This should only make the evolution in the  $M^*$  between the bins more significant. It is also important to mention that [Trenti & Stiavelli \(2008\)](#) have not considered baryonic feedback effects in their modelling, and their results may change if these effects are included. A large change in normalisation  $\phi^*$  value is seen with change in redshift, which can again be attributed to the large galaxy clusters in the redshift bin centered at  $z = 0.7$ . We would like to direct the reader's attention towards Table 4, which shows the relative error in the value of  $\phi^*$  calculated using methods suggested by [Trenti & Stiavelli \(2008\)](#) and [Moster et al. \(2010\)](#). These errors should be considered in addition to the total statistical errors quoted with the parameter values in Table 5.

We compare our UV LFs to the local UV LF calculated by [Wyder et al. \(2005\)](#) using *GALEX* FUV and NUV data. They obtained  $-18.04 \pm 0.11$  and  $-1.22 \pm 0.07$  for  $M^*$  and  $\alpha$  respectively for the FUV band. With respect to their findings our results at  $z = 0.7$  suggest an evolution in  $M^*$  best-fit values by 0.8 mag which is significant at  $4\sigma$ , from  $z = 0.7$  to the present time. This evolution can be seen in Fig. 11, where we plot the [Wyder et al. \(2005\)](#) results along with our results. As far as  $\alpha$  is concerned we do not see any significant change between  $z = 0.7$  and the local value.

The luminosity density of the Star forming galaxies is calculated by integrating the UV LF, and plotted in Fig. 13 along with values from other works. Our results for the luminosity density fall within the error regions of past studies, and follow the same trend as the redshift changes i.e. higher luminosity density at redshift  $z = 1$  as compared to its value at redshift  $z = 0.7$ .

We consider the effect of potential AGN contribution to our UV LF calculations. In order to do that, we create two source-lists. One by removing all potential AGN (these sources include all the sources identified by [Xue et al. \(2016\)](#) or [Luo et al. \(2017\)](#) as AGN and all sources with 0.5–8 KeV X-ray luminosity higher than  $10^{42}$  ergs  $s^{-1}$ ) from the sample. The second by including all these (potential AGN) sources in the final source-list. The distributions of the resulting two source-lists as a function of their  $M_{1500}$  magnitudes are plotted in Appendix A to show the contribution of these sources at the bright end of the luminosity function. We compare the Schechter function parameters obtained from both cases. The best-fit results for the case where all the identified AGN and bright X-ray sources are removed, stay within the  $1\sigma$  uncertainties of our actual result (obtained using the X-ray flux cut only). However, the values of LF parameters change drastically when all the potential AGN are included in the sample. The exact numbers for both cases are tabulated in the Table A1 and plotted in Fig. A1 in Appendix A. This result could also serve as an explanation to why we find a smaller number of bright galaxies as compared to [Hagen et al. \(2015\)](#). Even a small number of bright AGN present in their sample could brighten their characteristic magnitude by a significant amount, and consequently increase the luminosity density (Fig. 13).

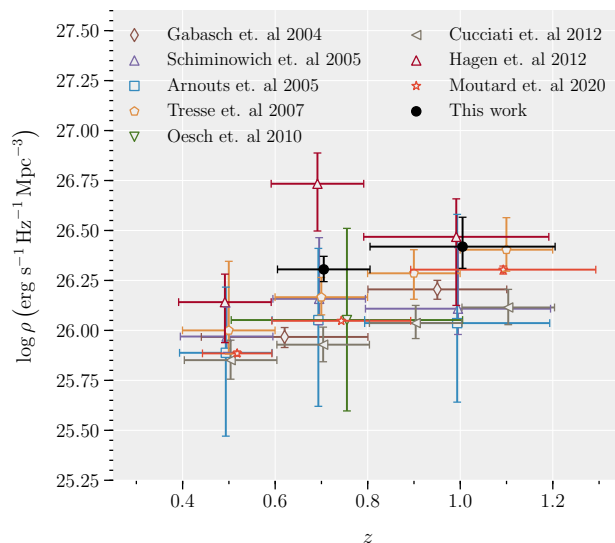


**Figure 13.** The luminosity density estimated by integrating the luminosity function. The data points in different colours represent the observed luminosity calculations from the following studies : [Gabasch et al. \(2004\)](#); [Schiminovich et al. \(2005\)](#); [Arnouts et al. \(2005\)](#); [Tresse et al. \(2007\)](#); [Oesch et al. \(2010\)](#); [Cucciati et al. \(2012\)](#); [Hagen et al. \(2015\)](#); [Moutard et al. \(2020\)](#). Our estimates are shown in black colour. The vertical and horizontal error bars represent the  $1\sigma$  (68.26 per cent) uncertainties and the redshift bin edges respectively. For clarity the data points at same redshifts are slightly moved.

## 11 SUMMARY AND CONCLUSION

We have measured the UV LF of galaxies over redshifts ranging from  $z = 0.6$  to  $z = 1.2$  using data from the XMM-EXTEND survey of the CDFS. Our estimates of the UV LF extend to deeper magnitudes than previous studies, with  $M_{1500} = [-20.75, -17.70]$  and  $[-21.60, -18.55]$  at  $0.6 \leq z < 0.8$  and  $0.8 \leq z < 1.2$ , respectively. We use Monte-Carlo simulations to estimate completeness of the data and the magnitude error distribution used to account for any photometric errors before the fitting process is executed. Using the [Page & Carrera \(2000\)](#) method, we construct binned realisations of the UV galaxy LF as a function of 1500 Å rest frame magnitudes in two redshift bins with average redshifts  $z = 0.7$  and  $z = 1.0$ .

The LF is well described by the Schechter function shape. We calculate the best-fit values of the galaxy LF parameters by fitting the Schechter function to the data by using parametric maximum-likelihood in both redshift bins. From our fits we obtain a relatively flat value of the faint-end slope  $\alpha = -1.10^{+0.19}_{-0.18}$  in the redshift range  $0.6 \leq z < 0.8$  compared with most previous studies, and in the redshift bin,  $0.8 \leq z < 1.2$  we obtain a best-fit value  $\alpha = -1.56^{+0.19}_{-0.18}$ . There is a small change in  $\alpha$  with low statistical significance between the two redshift bins.

Regarding the characteristic magnitude  $M_*$ , our derived values are 0.5 to 1 mag fainter than some previous studies in the same redshift ranges. Between the redshift bins under consideration,  $M_*$  also evolves by 0.8 mag at  $3\sigma$ .

The value of the characteristic number density  $\phi^*$  agrees with one of the previous works in the redshift bin centered



at  $z = 0.7$ . At  $z = 1$ , our estimate for  $\phi^*$  is within  $2\sigma$  of the closest value from literature. We attribute the differences to the cosmic variance of the different fields chosen by different works. Its values would be better constrained with estimates from different parts of the sky to counter the cosmic variance. The luminosity density for our sample is in agreement with the previous studies.

The AGN population in a galaxy sample can bias the UV LF parameters, if not handled properly. An effective way to remove the AGNs is using a total X-ray luminosity cut at  $10^{42}$  ergs  $s^{-1}$ .

The remarkable potential of the XMM-OM for this type of study is clear from the results so far. This OM data set with its observations of the CDFS has demonstrated already that it is a powerful tool for constraining the faint end of UV LF and thus exploring galaxy evolution to redshift 1. Further wide field data will provide critical insights into the bright end of the LF.

## 12 ACKNOWLEDGEMENTS

This research makes use of the observations taken with XMM-Newton telescope, an ESA science mission with instruments and contributions directly funded by ESA Member States and NASA. MJP acknowledges support from the UK Science and Technology Facility Council (STFC) grant number ST/S000216/1. MS would like to thank Vladimir Yershov for outstanding support with the XMM-OM software. MS also thanks Ignacio Ferreras, Paul Kuin and Sam Oates for valuable comments and discussions related to this manuscript. MS would like to extend their gratitude towards Michele Trenti for sharing the source code for their CV calculator. We thank the anonymous referee for their constructive report to further improve this manuscript.

## 13 DATA AVAILABILITY

The data used in this article can be obtained from the XMM-Newton Science archive (XSA) at <https://www.cosmos.esa.int/web/xmm-newton/xsa>. We make the source-list used in this paper as a supplementary table with the online version of the paper. Other supporting material related to this article is available on a reasonable request to the corresponding author.

## REFERENCES

- Aihara H., et al., 2018, *PASJ*, **70**, S4  
 Alavi A., et al., 2016, *ApJ*, **832**, 56  
 Antonucci M., Talavera A., Vagnetti F., Trevese D., Comastri A., Paolillo M., Ranalli P., Vignali C., 2015, *A&A*, **574**, A49  
 Arnouts S., et al., 2005, *ApJ*, **619**, L43  
 Balestra et al., 2010, *A&A*, **512**, A12  
 Behroozi P. S., Conroy C., Wechsler R. H., 2010, *ApJ*, **717**, 379  
 Benson A. J., Bower R. G., Frenk C. S., Lacey C. G., Baugh C. M., Cole S., 2003, *ApJ*, **599**, 38  
 Bhatawdekar R., Conselice C. J., Margalef-Bentabol B., Duncan K., 2019, *MNRAS*, **486**, 3805  
 Bouwens R. J., et al., 2015, *ApJ*, **803**, 34  
 Bower R. G., Benson A. J., Malbon R., Helly J. C., Frenk C. S., Baugh C. M., Cole S., Lacey C. G., 2006, *MNRAS*, **370**, 645  
 Bowler R. A. A., et al., 2015, *MNRAS*, **452**, 1817  
 Budavári T., et al., 2005, *ApJ*, **619**, L31  
 Cardamone C. N., et al., 2010, *ApJS*, **189**, 270  
 Cardelli J. A., Clayton G. C., Mathis J. S., 1989, *ApJ*, **345**, 245  
 Cattaneo A., et al., 2009, *Nature*, **460**, 213  
 Cole S., Lacey C. G., Baugh C. M., Frenk C. S., 2000, *MNRAS*, **319**, 168  
 Cole S., et al., 2001, *MNRAS*, **326**, 255  
 Comastri A., et al., 2011, *A&A*, **526**, L9  
 Croton D. J., et al., 2006, *MNRAS*, **365**, 11  
 Cucciati et al., 2012, *A&A*, **539**, A31  
 Dahlen T., Mobasher B., Dickinson M., Ferguson H. C., Giavalisco M., Kretchmer C., Ravindranath S., 2007, *ApJ*, **654**, 172  
 Dehghan S., Johnston-Hollitt M., 2014, *AJ*, **147**, 52  
 Dekel A., Silk J., 1986, *ApJ*, **303**, 39  
 Eddington A. S., 1913, *MNRAS*, **73**, 359  
 Fabian A. C., 2012, *ARA&A*, **50**, 455  
 Foreman-Mackey D., Hogg D. W., Lang D., Goodman J., 2013, *PASP*, **125**, 306  
 Gabasch A., et al., 2004, *A&A*, **421**, 41  
 Gaia Collaboration et al., 2018, *A&A*, **616**, A1  
 Gatto A., et al., 2017, *MNRAS*, **466**, 1903  
 Gehrels N., 1986, *ApJ*, **303**, 336  
 Gehrels N., et al., 2004, *ApJ*, **611**, 1005  
 Giacconi R., et al., 2001, *ApJ*, **551**, 624  
 Giavalisco M., et al., 2004, *ApJ*, **600**, L93  
 Gilli R., et al., 2003, *ApJ*, **592**, 721  
 Goodman J., Weare J., 2010, *Communications in Applied Mathematics and Computational Science*, **5**, 65  
 Hagen L. M. Z., Hoversten E. A., Gronwall C., Wolf C., Siegel M. H., Page M., Hagen A., 2015, *ApJ*, **808**, 178  
 Harrison C. M., Costa T., Tadhunter C. N., Flüttsch A., Kakkad D., Perna M., Vietri G., 2018, *Nature Astronomy*, **2**, 198  
 Hathi N. P., et al., 2010, *ApJ*, **720**, 1708  
 Hopkins P. F., Quataert E., Murray N., 2012, *MNRAS*, **421**, 3522  
 Hopkins P. F., Kereš D., Oñorbe J., Faucher-Giguère C.-A., Quataert E., Murray N., Bullock J. S., 2014, *MNRAS*, **445**, 581  
 Hsu L.-T., et al., 2014, *ApJ*, **796**, 60  
 Kennicutt R. C., Evans N. J., 2012, *ARA&A*, **50**, 531  
 King A., 2003, *ApJ*, **596**, L27  
 Kurk et al., 2013, *A&A*, **549**, A63  
 Le Fèvre et al., 2005, *A&A*, **439**, 845  
 Lehmer B. D., et al., 2005, *ApJS*, **161**, 21  
 Leitherer C., et al., 1999, *ApJS*, **123**, 3  
 Luo B., et al., 2008, *ApJS*, **179**, 19  
 Luo B., et al., 2017, *ApJS*, **228**, 2  
 Ly C., et al., 2009, *ApJ*, **697**, 1410  
 Madau P., Dickinson M., 2014, *ARA&A*, **52**, 415  
 Martin D. C., et al., 2005, *ApJ*, **619**, L1  
 Mason K. O., et al., 2001, *A&A*, **365**, L36  
 Mehta V., et al., 2017, *ApJ*, **838**, 29  
 Mignoli, M. et al., 2005, *A&A*, **437**, 883  
 Morrissey P., et al., 2007, *ApJS*, **173**, 682  
 Moster B. P., Somerville R. S., Maulbetsch C., van den Bosch F. C., Macciò A. V., Naab T., Oser L., 2010, *ApJ*, **710**, 903  
 Moster B. P., Somerville R. S., Newman J. A., Rix H.-W., 2011, *ApJ*, **731**, 113  
 Moutard T., Sawicki M., Arnouts S., Golob A., Coupon J., Ilbert O., Yang X., Gwyn S., 2020, *MNRAS*, **494**, 1894  
 Murray N., Quataert E., Thompson T. A., 2005, *ApJ*, **618**, 569  
 Oesch P. A., et al., 2010, *ApJ*, **725**, L150  
 Oke J. B., Gunn J. E., 1983, *ApJ*, **266**, 713  
 Oppenheimer B. D., Davé R., 2006, *MNRAS*, **373**, 1265  
 Ouchi M., et al., 2009, *ApJ*, **706**, 1136  
 Page M. J., Carrera F. J., 2000, *MNRAS*, **311**, 433  
 Page M. J., et al., 2012, *MNRAS*, **426**, 903  
 Page M. J., et al., 2017, *MNRAS*, **466**, 1061

- Page M. J., et al., 2021, *MNRAS*, **506**, 473
- Parsa S., Dunlop J. S., McLure R. J., Mortlock A., 2016, *MNRAS*, **456**, 3194
- Pych W., 2004, *PASP*, **116**, 148
- Rafferty D. A., Brandt W. N., Alexander D. M., Xue Y. Q., Bauer F. E., Lehmer B. D., Luo B., Papovich C., 2011, *ApJ*, **742**, 3
- Ravikumar et al., 2007, *A&A*, **465**, 1099
- Roming P. W. A., et al., 2005, *Space Sci. Rev.*, **120**, 95
- Rosati P., et al., 2002, *ApJ*, **566**, 667
- Santini P., et al., 2015, *ApJ*, **801**, 97
- Sawicki M., et al., 2019, *MNRAS*, **489**, 5202
- Schechter P., 1976, *ApJ*, **203**, 297
- Schimminovich D., et al., 2005, *ApJ*, **619**, L47
- Schlafly E. F., Finkbeiner D. P., 2011, *ApJ*, **737**, 103
- Schlegel D. J., Finkbeiner D. P., Davis M., 1998, *ApJ*, **500**, 525
- Sheth R. K., Tormen G., 1999, *MNRAS*, **308**, 119
- Silk J., Rees M. J., 1998, *A&A*, **331**, L1
- Silverman J. D., et al., 2010, *The Astrophysical Journal Supplement Series*, **191**, 124
- Somerville R. S., Davé R., 2015, *ARA&A*, **53**, 51
- Somerville R. S., Lee K., Ferguson H. C., Gardner J. P., Moustakas L. A., Giavalisco M., 2004, *ApJ*, **600**, L171
- Springel V., Hernquist L., 2003, *MNRAS*, **339**, 312
- Stark A. A., Gammie C. F., Wilson R. W., Bally J., Linke R. A., Heiles C., Hurwitz M., 1992, *ApJS*, **79**, 77
- Stefanon M., et al., 2017, *ApJ*, **851**, 43
- Szokoly G. P., et al., 2004, *ApJS*, **155**, 271
- Taylor E. N., et al., 2009, *ApJS*, **183**, 295
- Trenti M., Stiavelli M., 2008, *ApJ*, **676**, 767
- Tresse L., et al., 2007, *A&A*, **472**, 403
- Vanzella et al., 2008, *A&A*, **478**, 83
- Weisz D. R., Johnson B. D., Conroy C., 2014, *ApJ*, **794**, L3
- White S. D. M., Frenk C. S., 1991, *ApJ*, **379**, 52
- Wolf C., et al., 2004, *A&A*, **421**, 913
- Wolf Hildebrandt, H. Taylor, E. N. Meisenheimer, K. 2008, *A&A*, **492**, 933
- Wuyts S., Labbé I., Förster Schreiber N. M., Franx M., Rudnick G., Brammer G. B., van Dokkum P. G., 2008, *ApJ*, **689**, 653
- Wyder T. K., et al., 2005, *ApJ*, **619**, L15
- Xue Y. Q., Luo B., Brandt W. N., Alexander D. M., Bauer F. E., Lehmer B. D., Yang G., 2016, *ApJS*, **224**, 15
- Yang X., Mo H. J., van den Bosch F. C., 2003, *MNRAS*, **339**, 1057
- Yoshida M., et al., 2006, *ApJ*, **653**, 988

## APPENDIX A: AGN IN THE SAMPLE

As mentioned in section 4.2, the X-ray sources are identified after cross-correlating our source-list with Xue et al. (2016) and Luo et al. (2017) catalogues. In our overall source-list of 2581 sources, 99 are identified as X-ray sources, 63 of which have a 0.5 – 8 KeV X-ray luminosity higher than  $10^{42}$  ergs  $s^{-1}$ . We only consider these 63 bright sources as the ones that may host powerful enough AGN, such that the UV radiation coming from an accretion disc around their supermassive black holes dominates over any coming from the star formation activity. These can contaminate our source-list and hamper the UV LF calculations. 17 of these bright X-ray sources fall in the  $0.6 \leq z < 0.8$  redshift bin, and have  $M_{1500}$  absolute magnitude in the range  $[-23.65, -18.62]$ . In the redshift bin  $0.8 \leq z < 1.2$ , 11 bright X-ray sources are identified with this criteria with  $M_{1500} = [-24.17, -19.95]$ . The distributions of the identified X-ray sources are plotted in Fig. A1.

Here we look at the effects on the results if : 1) We

**Table A1.** The best-fit values of the fitted Schechter function parameters for both redshift bins in our study, for the two cases discussed in the text.

$\langle z \rangle$	$M^*$	$\alpha$
All AGN included		
0.7 <sup>a</sup>	−20.22	−2.05
1.0 <sup>a</sup>	−21.56	−2.51
All AGN removed		
0.7 <sup>a</sup>	−18.90	−1.16
1.0 <sup>a</sup>	−19.72	−1.65

<sup>a</sup>Average redshift for the bin.

remove all the identified X-ray sources, which would mean removing more AGN at the expense of excluding some star-forming galaxies without an AGN as well. This case in our survey effectively brings the X-ray luminosity cut down to  $\sim 10^{41}$  ergs  $s^{-1}$ . 2) We do not remove any of the identified X-ray source, and compare these two cases with our actual results which have been obtained by removing only the bright X-ray sources using a luminosity cut. In table A1, we have the values of faint-end slope and characteristic magnitude for both these cases, and in Fig. A2 we plot these parameter values to compare with our estimates based on a sample with only bright X-ray sources removed.

It is apparent from Fig. A2 that the small amount of perturbation in the final results are within the  $1\sigma$  error region if all the sources which are potential AGN, are removed from the sample. However, if all these sources are included, the values of both the parameters namely faint-end slope and characteristic magnitude change by a large margin. The  $M^*$  value brightens by more than a magnitude for  $z = 0.7$ , and by almost 2 magnitudes for average redshift  $z = 1$ , as compared to our final results for  $M^*$  tabulated in table 5. This is expected, as there are sources with UV absolute magnitudes reaching  $-24$  mag as mentioned in the first paragraph (Fig. A1). These very bright sources affect the bright end of the LF where there are very few or no galaxies at all. The brighter values of characteristic magnitude drag the faint end slope to extremely steep numbers because of a strong correlation between these two parameters.

So we conclude that the bright AGN, if not treated properly can impact the final UV LF parameters. Their absence from the sample still does not change the parameters significantly with respect to those obtained if the X-ray luminosity cut is applied to the source-list removing only the bright X-ray sources. But, their presence, even in small numbers can significantly change the estimated parameters and distort the shape of the UV LF.

This paper has been typeset from a  $\text{\TeX}/\text{\LaTeX}$  file prepared by the author.

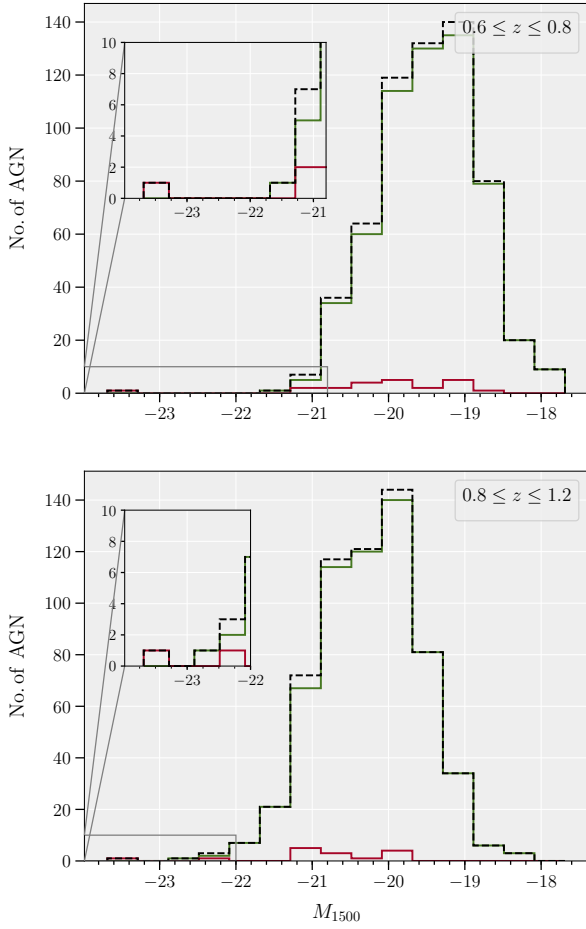


**Figure A1.** We show here the distribution of sources in our sample as a function of  $M_{1500}$  absolute magnitude. The top and bottom panels show the distribution in redshift bins  $z = 0.7$  and  $z = 1.0$  respectively. The red histogram represents the X-ray sources with luminosity  $10^{42}$  ergs  $s^{-1}$  and sources identified as AGN in [Xue et al. \(2016\)](#) and [Luo et al. \(2017\)](#) X-ray catalogues from CDFS. The histogram in green shows the source-list with all the sources in the red distribution removed. The distribution in black represents the total source-list including all the Star-forming galaxies and identified X-ray sources. The inset figures in each panel show the distribution at bright ends stretched along the y-axis.

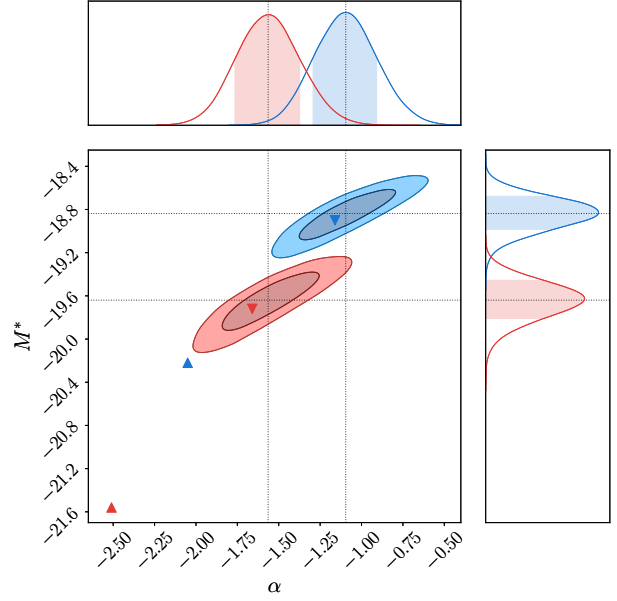


**Figure A2.** This figure is the same as Fig. 10, except that we also plot the values tabulated in Table A1. The coloured contours have the same meaning as in Fig. 10, with the dotted lines representing values calculated in this work. The upward triangles represent values obtained by including all the AGN in the sample and the downward triangles show the parameters obtained with a sample including no AGNs at all. The red triangles correspond to the red contour representing the redshift bin  $0.6 \leq z < 0.8$  and the ones in blue color representing the bin  $0.8 \leq z < 1.2$ .